PHYSICAL REVIEW D **109,** 084014 (2024)

Gravitational lensing by Born-Infeld naked singularities

Yiqian Chen,[1,*] Peng Wang,[1,†] Houwen Wu,[1,2,‡] and Haitang Yang[1,§]
[1]*Center for Theoretical Physics, College of Physics, Sichuan University, Chengdu 610064, China*
[2]*Department of Applied Mathematics and Theoretical Physics, University of Cambridge,*
Wilberforce Road, Cambridge CB3 0WA, United Kingdom

(Received 4 July 2023; accepted 14 March 2024; published 8 April 2024)

We examine the gravitational lensing phenomenon caused by photon spheres in the Born-Infeld naked singularity spacetime, where gravity is coupled with Born-Infeld electrodynamics. Specifically, our focus lies on relativistic images originating from a pointlike light source generated by strong gravitational lensing near photon spheres, as well as images of a luminous celestial sphere. It shows that Born-Infeld naked singularities consistently exhibit one or two photon spheres, which project onto one or two critical curves on the image plane. Our analysis reveals that when appropriately regularized, the singularity allows photons entering the photon sphere(s) to traverse it. This, in turn, leads to the emergence of new relativistic images within the innermost critical curve. Furthermore, the presence of two photon spheres doubles the number of relativistic images compared to the scenario with only a single photon sphere. Additionally, the transparency inherent to Born-Infeld naked singularities results in the absence of a central shadow in the images of celestial spheres.

DOI: 10.1103/PhysRevD.109.084014

I. INTRODUCTION

Gravitational lensing, the phenomenon of light bending in curved space, is a captivating and fundamental effect predicted by general relativity [1–3]. Due to its pivotal role in astrophysics and cosmology, extensive research has been conducted on gravitational lensing in the past decades. It has contributed significantly to addressing crucial topics such as the distribution of structures [4–6], dark matter [7–9], dark energy [10–13], quasars [14–17], and gravitational waves [18–20]. In an idealized lens model involving a distant source in a Schwarzschild black hole, the slight deflection of light in a weak gravitational field gives rise to the observation of a primary and a secondary image. Moreover, strong gravitational lensing near the photon sphere generates an infinite sequence of higher-order images, known as relativistic images, on both sides of the optic axis [21]. Remarkably, relativistic images are minimally affected by the characteristics of the astronomical source, making them valuable for investigating the nature of the black hole spacetime.

Recently, the remarkable achievement of high angular resolution by the Event Horizon Telescope (EHT) Collaboration [22–35], has facilitated the study of gravitational lensing in the strong gravity regime, reigniting interest in the shadow of black hole images and the associated phenomenon of strong gravitational lensing [36–71]. It has been demonstrated that strong gravitational lensing exhibits a close connection to bound photon orbits, which give rise to photon spheres in spherically symmetric black holes. Intriguingly, certain horizonless ultracompact objects have been discovered to harbor photon spheres, effectively mimicking black holes in numerous observational simulations [72–82]. Among these objects, naked singularities have garnered significant attention. Although the cosmic censorship conjecture forbids the formation of naked singularities, it is possible for these entities to arise through the gravitational collapse of massive objects under specific initial conditions [83–89]. Given that the presence of photon spheres allows naked singularities to emulate the optical appearance of black holes, the gravitational lensing phenomena associated with naked singularities have been extensively investigated [90–97].

In the context of Reissner-Nordström (RN) naked singularities characterized by a mass M and charge Q, it is noteworthy that a photon sphere exists only if $1 < Q/M \leq \sqrt{9/8}$, whereas no photon sphere is present when $Q/M > \sqrt{9/8}$. The phenomenon of strong gravitational lensing by the photon sphere has been investigated within the spacetime of RN naked singularities [95,97]. Analogous to the case of black holes, two sets of relativistic images can be observed beyond the critical curve, which arises from photons originating from the photon sphere. Remarkably, two additional sets of brighter relativistic images have been identified within the critical curve due

---

[*] yqchen@stu.scu.edu.cn
[†] pengw@scu.edu.cn
[‡] hw598@damtp.cam.ac.uk
[§] hyanga@scu.edu.cn

to the absence of an event horizon and the existence of a potential barrier near the antiphoton sphere. Furthermore, as demonstrated below, when a celestial sphere illuminates an RN naked singularity, the absence of a shadow at the center of the image is observed since light rays entering the photon sphere are reflected by the potential barrier at the singularity. These distinctive observational characteristics can serve as means to differentiate between RN singularities and RN black holes.

The Born-Infeld electrodynamics was initially proposed to regulate the divergences arising from the electrostatic self-energy of point charges, achieved through the introduction of an electric field cutoff [98]. Subsequently, it was recognized that Born-Infeld electrodynamics can emerge from the low-energy limit of string theory, which describes the dynamics of D-branes at low energies. Coupling the Born-Infeld electrodynamics field to gravity, the Born-Infeld black hole solution was obtained in [99,100]. Since then, a multitude of properties pertaining to Born-Infeld black holes have been extensively examined [101–113]. More recently, it has been reported that Born-Infeld naked singularity solutions can exhibit two photon spheres within specific parameter ranges [114].

The primary objective of this paper is to investigate gravitational lensing phenomena exhibited by Born-Infeld naked singularities. Remarkably, our findings unveil the ability of photons to traverse these singularities, which, in conjunction with the presence of double photon spheres, gives rise to distinct observational signatures. The subsequent sections of this paper are structured as follows. In Sec. II, we provide a concise overview of the Born-Infeld naked singularity solution and present their domain of existence. Section III focuses on the analysis of photon trajectories in an effective geometry and explores their behavior in proximity to the singularity. In Sec. IV, after the naked singularity is regularized with a regular core, we derive the deflection angle of light rays traversing the core and establish connection formulas between the ingoing and outgoing branches of their trajectories within the singularity spacetime. The discussion then proceeds to examine relativistic images of a distant light source in Sec. V, followed by the analysis of images produced by a luminous celestial sphere in Sec. VI. Finally, Sec. VII presents our conclusions. We adopt the convention $G = c = 1$ throughout the paper.

II. BORN-INFELD NAKED SINGULARITY

We consider a $(3+1)$-dimensional gravity model coupled to a Born-Infeld electromagnetic field A_μ. The action $\mathcal{S}$ is given by

$$\mathcal{S} = \frac{1}{16\pi}\int d^4x\sqrt{-g}\left[R + 4\mathcal{L}(s,p)\right], \tag{1}$$

where

$$\mathcal{L}(s,p) = \frac{1}{a}\left(1 - \sqrt{1 - 2as - a^2p^2}\right). \tag{2}$$

Here, s and p are two independent nontrivial scalars constructed from the field strength tensor $F_{\mu\nu} = \partial_\mu A_\nu - \partial_\nu A_\mu$ and none of its derivatives, i.e.,

$$s = -\frac{1}{4}F^{\mu\nu}F_{\mu\nu} \quad \text{and} \quad p = -\frac{1}{8}\epsilon^{\mu\nu\rho\sigma}F_{\mu\nu}F_{\rho\sigma}, \tag{3}$$

where $\epsilon^{\mu\nu\rho\sigma} \equiv -[\mu\,\nu\,\rho\,\sigma]/\sqrt{-g}$ is a totally antisymmetric Lorentz tensor, and $[\mu\,\nu\,\rho\,\sigma]$ denotes the permutation symbol. The coupling parameter a is related to the string tension α' as $a = (2\pi\alpha')^2$. In the limit $a \to 0$, the Born-Infeld Lagrangian $\mathcal{L}(s,p)$ reduces to the Lagrangian of the Maxwell field. The equations of motion can be obtained by varying the action (1) with respect to $g_{\mu\nu}$ and A_μ, yielding

$$R_{\mu\nu} - \frac{1}{2}Rg_{\mu\nu} = \frac{T_{\mu\nu}}{2},$$
$$\nabla_\mu\left[\frac{\partial\mathcal{L}(s,p)}{\partial s}F^{\mu\nu} + \frac{1}{2}\frac{\partial\mathcal{L}(s,p)}{\partial p}\epsilon^{\mu\nu\rho\sigma}F_{\rho\sigma}\right] = 0, \tag{4}$$

where $T_{\mu\nu}$ is the energy-momentum tensor,

$$T_{\mu\nu} = 4g_{\mu\nu}\left[\mathcal{L}(s,p) - p\frac{\partial\mathcal{L}(s,p)}{\partial p}\right] + \frac{\partial\mathcal{L}(s,p)}{\partial s}F_\mu{}^\rho F_{\nu\rho}. \tag{5}$$

The spherically symmetric ansatz yields a solution to the equations of motion (4) [99,100,114]. The metric is given by

$$\begin{aligned} ds^2 &= g_{\mu\nu}dx^\mu dx^\nu \\ &= -f_{\mathrm{BI}}(r)dt^2 + \frac{dr^2}{f_{\mathrm{BI}}(r)} + r^2(d\theta^2 + \sin^2\theta d\varphi^2), \\ A &= A_t(r)dt - P\cos\theta d\varphi, \end{aligned} \tag{6}$$

where

$$\begin{aligned} f_{\mathrm{BI}}(r) &= 1 - \frac{2M}{r} - \frac{2(Q^2+P^2)}{3\sqrt{r^4 + a(Q^2+P^2)} + 3r^2} \\ &\quad + \frac{4(Q^2+P^2)}{3r^2}\,{}_2F_1\left(\frac{1}{4},\frac{1}{2},\frac{5}{4};-\frac{a(Q^2+P^2)}{r^4}\right), \\ A_t'(r) &= \frac{Q}{\sqrt{r^4 + a(Q^2+P^2)}}. \end{aligned} \tag{7}$$

The mass, electrical charge, and magnetic charge of the black hole are denoted by M, Q and P, respectively, and ${}_2F_1(a,b,c;x)$ is the hypergeometric function. Moreover, the solution appears to have a singularity at $r = 0$. The nature of the singularity is investigated using the Kretschmann scalar $\mathcal{K} = R^{\mu\nu\rho\sigma}R_{\mu\nu\rho\sigma}$. Our calculation reveals that the origin is a physical singularity as

$$\mathcal{K} = 48\left(\frac{\Gamma^2(1/4)[a(P^2+Q^2)]^{3/4}}{6a\sqrt{\pi}} - M\right)^2 r^{-6} + \mathcal{O}(r^{-5}). \tag{8}$$

Thus, the solution (6) describes a naked singularity at $r = 0$ or a black hole if an event horizon exists.

To determine the separatrix between naked singularity and black hole solutions, we investigate extremal black holes with horizon radius r_e and mass M_e. The conditions $f(r_e) = 0 = d(rf(r))/dr|_{r=r_e}$ yield the expressions for r_e and mass M_e as

$$\begin{aligned} r_e &= \frac{\sqrt{4(Q^2+P^2)-a}}{2}, \\ M_e &= \frac{\sqrt{4(Q^2+P^2)-a}}{6} + \frac{8(Q^2+P^2)}{6\sqrt{4(Q^2+P^2)-a}} \\ &\quad \times {}_2F_1\left(\frac{1}{4},\frac{1}{2};\frac{5}{4};-\frac{16a(Q^2+P^2)}{[4(Q^2+P^2)-a]^2}\right). \end{aligned} \tag{9}$$

It is evident that extremal black holes do not exist for $a > 4(Q^2+P^2)$. So when $a < 4(Q^2+P^2)$ and $M < M_e$, the spacetime is a naked singularity. However, when $a > 4(Q^2+P^2)$, the spacetime can have at most one horizon. The presence of the horizon can be determined by investigating $rf(r)$, which vanishes at the horizon radius. In fact, one finds $d(rf(r))/dr > 0$ and $\lim_{r\to 0} rf(r) = 4[a(Q^2+P^2)]^{3/4}\Gamma(1/4)\Gamma(5/4)/(3a\sqrt{\pi}) - 2M$, indicating the appearance of a naked singularity when

$$M < \frac{\Gamma^2(1/4)[a(P^2+Q^2)]^{3/4}}{6a\sqrt{\pi}}. \tag{10}$$

The left panel of Fig. 1 shows the domain of existence for Born-Infeld naked singularities in the $a/M^2 - \sqrt{Q^2+P^2}/M$ parameter space, with the dashed black line denoting the separatrix between the black hole and naked singularity solutions. Solutions above the dashed black line in the colored regions represent Born-Infeld naked singularities.

III. PHOTON TRAJECTORIES

Nonlinear electrodynamics theories allow for self-interaction of the electromagnetic field, leading to changes in the direction of photon propagation and deviation from

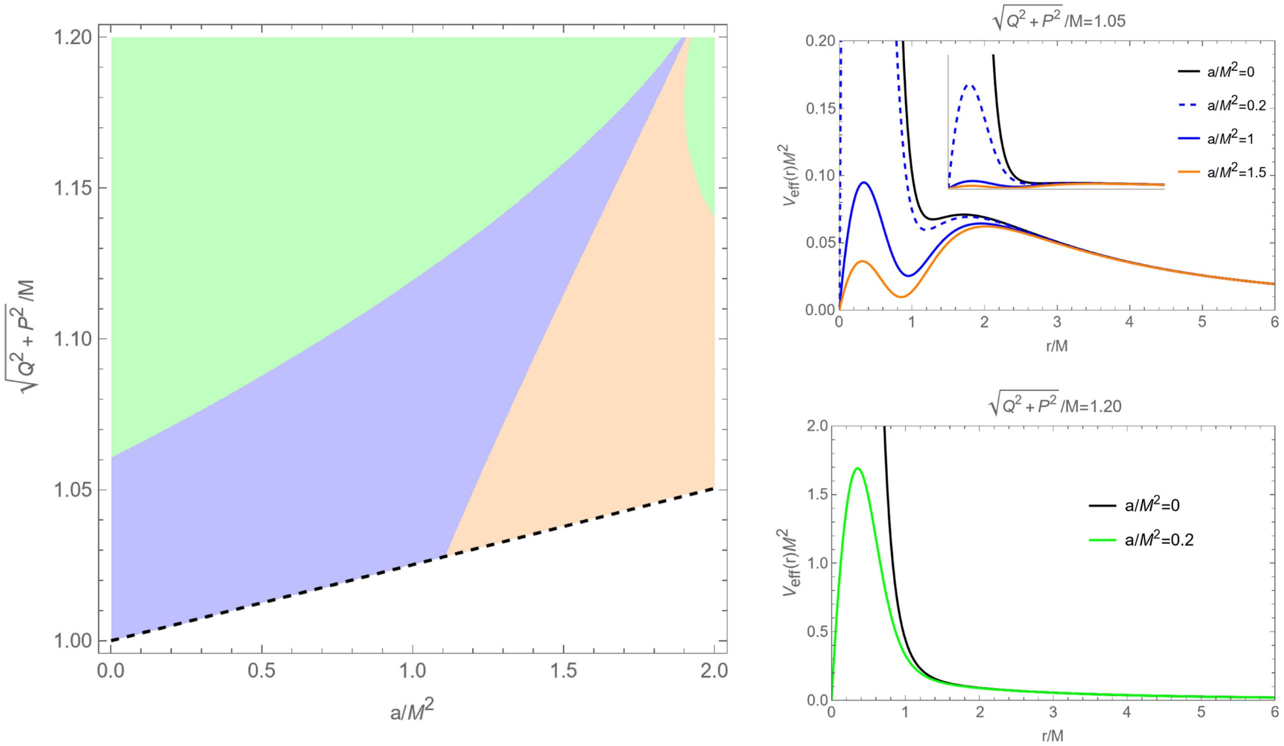

FIG. 1. Left: The Born-Infeld metric (6) above the dashed black line describes a naked singularity at $r = 0$. Within the blue and orange regions, naked singularity solutions have two photon spheres, and the effective potential at the inner photon sphere is higher/lower than that at the outer one in the blue/orange regions. The solutions in the green region have only one photon sphere. Right: The upper and lower panels show the effective potential $V_{\rm eff}(r)$ of representative naked singularity solutions with $Q = 1.05$ and 1.20, respectively. A photon sphere corresponds to a local maximum of $V_{\rm eff}(r)$.

null geodesics. Propagation equations describing photon trajectories can be obtained by analyzing the electromagnetic field's discontinuity at the characteristic surface of wave propagation. An effective metric is then introduced, in which photons travel on null geodesics [115]. In one-parameter theories with the Lagrangian as a function of s, a single effective geometry determines the photon trajectories. However, in two-parameter theories with the Lagrangian as a function of s and p, two possible solutions exist, leading to birefringence. The Born-Infeld theory, on the other hand, ensures the uniqueness of the photon path via its equations of motion, and the effective metric $\tilde{g}^{\mu\nu}$ is given by [115]

$$\tilde{g}^{\mu\nu} = \frac{(1-2as)g^{\mu\nu} + a g_{\rho\sigma}F^{\mu\rho}F^{\sigma\nu}}{(1-2as-a^2p^2)^{3/2}}. \tag{11}$$

Using the underlying Born-Infeld metric (6), the effective metric takes the form

$$\begin{aligned} d\tilde{s}^2 &= \tilde{g}_{\mu\nu}dx^\mu dx^\nu = -f(r)dt^2 + \frac{dr^2}{h(r)} + R(r)(d\theta^2 + \sin^2\theta d\varphi^2) \\ &= \frac{(aP^2+r^4)^2}{r^2[a(Q^2+P^2)+r^4]^{3/2}}\left[-f_{\mathrm{BI}}(r)dt^2 + \frac{dr^2}{f_{\mathrm{BI}}(r)} + \frac{a(Q^2+P^2)+r^4}{r^2}(d\theta^2+\sin^2\theta d\varphi^2)\right], \end{aligned} \tag{12}$$

where $\tilde{g}_{\mu\rho}\tilde{g}^{\rho\nu} = \delta^\nu_\mu$, and

$$\begin{aligned} f(r) &= \frac{(aP^2+r^4)^2}{r^2[a(Q^2+P^2)+r^4]^{3/2}} f_{\mathrm{BI}}(r), \\ h(r) &= \frac{r^2[a(Q^2+P^2)+r^4]^{3/2}}{(aP^2+r^4)^2} f_{\mathrm{BI}}(r), \\ R(r) &= \frac{(aP^2+r^4)^2}{r^4\sqrt{a(Q^2+P^2)+r^4}}. \end{aligned} \tag{13}$$

Although the effective metric appears to lack electric-magnetic duality, this symmetry is present when the metric is multiplied by a conformal factor $(aP^2+r^4)^{-2}$, which does not alter null geodesics. Therefore, the electric-magnetic duality of photon trajectories is expected. Furthermore near $r=0$, the Kretschmann scalar of the effective metric diverges as

$$\mathcal{K} = \frac{1488}{a(P^2+Q^2)}\left(\frac{\Gamma^2(1/4)[a(P^2+Q^2)]^{3/4}}{6a\sqrt{\pi}} - M\right)^2 r^{-2} + \mathcal{O}(r^{-1}), \tag{14}$$

indicating the persistence of $r=0$ as a singularity in the effective metric. As anticipated, the Penrose diagram of the effective metric coincides with that of the Born-Infeld naked singularity metric, which is depicted in the left panel of Fig. 2.

In the Hamiltonian canonical formalism, a photon with 4-momentum vector $p^\mu = (\dot{t}, \dot{r}, \dot{\theta}, \dot{\varphi})$, where dots stand for derivative with respect to some affine parameter λ, has canonical momentum $q_\mu = \tilde{g}_{\mu\nu}p^\nu$, which satisfies the null condition $p^\mu q_\mu = 0$. The null geodesic equations in the effective metric (12) are separable and can be fully characterized by three conserved quantities,

$$\begin{aligned} E = q_\mu \partial^\mu_t = -q_t, \qquad L_z = q_\mu \partial^\mu_\varphi = q_\varphi, \\ L^2 = K^{\mu\nu}q_\mu q_\nu = q_\theta^2 + L_z^2\csc^2\theta, \end{aligned} \tag{15}$$

which denote the total energy, the angular momentum parallel to the axis of symmetry, and the total angular momentum, respectively. Here, the tensor $K^{\mu\nu}$ is an symmetric Killing tensor,

$$K = R^2(r)(d\theta \otimes d\theta + \sin^2\theta d\varphi \otimes d\varphi). \tag{16}$$

Note that $\tilde{\nabla}_{(\lambda}K_{\mu\nu)} = 0$, where $\tilde{\nabla}$ is the covariant derivative compatible with the effective metric. The canonical 4-momentum $q = q_\mu dx^\mu$ can be expressed in terms of E, L_z and L as

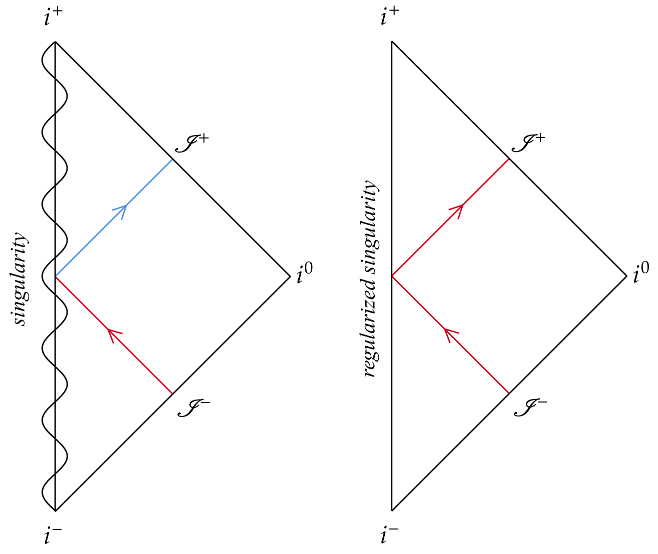

FIG. 2. Penrose diagrams for the Born-Infeld naked singularity (left) and the regularized Born-Infeld singularity with a regular core (right).

$$q=-Edt\pm_r\sqrt{\mathcal{R}(r)}dr\pm_\theta\sqrt{\Theta(\theta)}d\theta+Ld\varphi,$$
$$\mathcal{R}(r)=\frac{1}{h(r)}\left(\frac{E^2}{f(r)}-\frac{L^2}{R(r)}\right)\ \text{and}\ \Theta(\theta)=L^2-L_z^2\csc^2\theta, \tag{17}$$

where the two choices of sign $\pm_r$ and $\pm_\theta$ depend on the radial and polar directions of travel, respectively. Then, null geodesic equations are given by $p^\mu=\tilde{g}^{\mu\nu}q_\nu$, i.e.,

$$\dot{t}=\frac{E}{f(r)},\qquad \dot{r}=\pm_r L\sqrt{\frac{h(r)}{f(r)}[b^{-2}-V_{\text{eff}}(r)]},$$
$$\dot{\theta}=\pm_\theta\frac{\sqrt{L^2-L_z^2\csc^2\theta}}{R(r)},\qquad \dot{\varphi}=\frac{L_z}{R(r)\sin^2(\theta)}, \tag{18}$$

where $b\equiv L/E$ is the impact parameter, and the effective potential of photons in the effective metric is defined as

$$V_{\text{eff}}(r)=\frac{f(r)}{R(r)}. \tag{19}$$

While black hole studies typically neglect the near-singularity behavior of photons within the horizon, the absence of an event horizon in naked singularities necessitates analyzing photon behavior near their singularities. In the Born-Infeld naked singularity spacetime, the effective potential for photons approaches zero at $r=0$,

$$V_{\text{eff}}(r)=2a(P^2+Q^2)\left(\frac{\Gamma^2(1/4)[a(P^2+Q^2)]^{3/4}}{6a\sqrt{\pi}}-M\right)r+\mathcal{O}(r^2), \tag{20}$$

indicating their ability to reach the singularity. However, the effective potential for null geodesics in the Born-Infeld metric diverges at $r=0$,

$$V_{\text{eff}}(r)=2\left(\frac{\Gamma^2(1/4)[a(P^2+Q^2)]^{3/4}}{6a\sqrt{\pi}}-M\right)r^{-3}+\mathcal{O}(r^{-2}), \tag{21}$$

precluding their arrival at the singularity. This observation underscores that the nonlinear nature of Born-Infeld electrodynamics permits photons to reach the singularity, prompting investigations into photon trajectories near the singularity. Specifically, Eq. (18) gives the behavior of photons around the singularity at $r=0$, yielding

$$\frac{dr}{dt}=\pm_r 2\left(\frac{\Gamma^2(1/4)[a(P^2+Q^2)]^{3/4}}{6a\sqrt{\pi}}-M\right)r^{-1}+\mathcal{O}(r^0). \tag{22}$$

Equation (22) carries a twofold implication: first, photons originating from distant sources reach the singularity in a finite coordinate time, and second, photons departing from the singularity reach distant observers within a finite coordinate time.

Furthermore, we find that, near the singularity, solutions of the null geodesic equations (18) can be expanded as

$$x^\mu=x_0^\mu+\sum_{n=1}^{\infty}\sum_{m=0}^{n-1}c_{nm}^\mu\lambda^{-n}\log^m|\lambda|\quad\text{for}\ \mu=t,r,\theta\ \text{and}\ \varphi, \tag{23}$$

where x_0^μ are the constant of integration, and the coefficients c_{nm}^μ are calculated recursively order by order. Particularly, the leading coefficients are given by

$$c_{20}^t=\pm_r\frac{3\sqrt{\pi}a^{5/4}(Q^2+P^2)}{2\Gamma^2(1/4)(Q^2+P^2)^{3/4}E^2-12\sqrt{\pi}a^{1/4}E^2M},\qquad c_{10}^r=\mp_r\frac{\sqrt{a(Q^2+P^2)}}{E},$$
$$c_{30}^\theta=\mp_\theta\frac{\sqrt{a(Q^2+P^2)}\sqrt{L^2-L_z^2\csc^2x_0^\theta}}{3E^4},\qquad c_{30}^\varphi=-\frac{\sqrt{a(Q^2+P^2)}L_z\csc^2x_0^\theta}{3E^4}. \tag{24}$$

It shows the existence of two branches of light rays; the radially outgoing one associated with the upper sign of $\pm_r$ and $\mp_r$, and the radially ingoing one with the lower sign. We adopt $\lambda>0$ and $\lambda<0$ for the ingoing and outgoing branches, respectively. It is worth emphasizing that the affine parameter approaches $\pm\infty$ when the light ray approaches the singularity, leading to $x_0^r=0$. The left panel of Fig. 2 illustrates the ingoing and outgoing branches, denoted by red and blue lines, respectively, in the Penrose diagram of the Born-Infeld naked singularity.

The effective potential $V_{\text{eff}}(r)$ determines the locations of circular light rays, with unstable and stable light rays corresponding to local maxima and minima, respectively. The unstable circular light rays form photon spheres, which are critical for observing black holes. From Eq. (12), it follows that $V_{\text{eff}}(\infty)=0=V_{\text{eff}}(0)$ when $a>0$, indicating the existence of at least one photon sphere in the Born-Infeld naked singularity spacetime. The left panel of Fig. 1 illustrates the regions where one or two photon spheres exist in the $a/M^2-\sqrt{Q^2+P^2}/M$ parameter space:

(i) The green region corresponds to a single photon sphere in the naked singularity spacetime, as illustrated by the green line in the lower-right panel of Fig. 1 for $V_{\mathrm{eff}}(r)$ with $\sqrt{Q^2+P^2}/M = 1.20$ and $a/M^2 = 0.2$.

(ii) The blue regions correspond to naked singularities with two photon spheres, as illustrated by the blue lines in the upper-right panel of Fig. 1 for $V_{\mathrm{eff}}(r)$ with $\sqrt{Q^2+P^2}/M = 1.05$ and $a/M^2 = 0.2$ and 1. The potential peak at the inner photon sphere is higher than that at the outer one, indicating that both photon spheres play a role in determining the optical appearances of luminous matters [116–119].

(iii) The orange regions correspond to naked singularities with two photon spheres, as illustrated by the orange line in the upper-right panel of Fig. 1 for $V_{\mathrm{eff}}(r)$ with $\sqrt{Q^2+P^2}/M = 1.05$ and $a/M^2 = 1.5$. The potential peak at the inner photon sphere is lower than that at the outer one. In this case, the inner photon sphere is invisible to distant observers since light rays near it can not escape to infinity. Nevertheless, the inner photon sphere is closely related to long-lived quasinormal modes [120], echo signals [121] and superradiant instability [122].

The effective potential $V_{\mathrm{eff}}(r)$ of RN naked singularities with $a = 0$ possesses a photon sphere provided that $1 < \sqrt{Q^2+P^2}/M < \sqrt{9/8}$ (e.g., indicated by the black line in the upper-right panel of Fig. 1), while no photon sphere exists when $\sqrt{Q^2+P^2}/M \geq \sqrt{9/8}$ (e.g., the black line in the lower-right panel of Fig. 1) [123]. In addition, $V_{\mathrm{eff}}(r)$ diverges at $r = 0$ for RN naked singularities, preventing photons from approaching the singularity. Interestingly, when the effects of nonlinear electrodynamics are present, $V_{\mathrm{eff}}(r)$ approaches zero instead of infinity as $r \to 0$, enabling photons with a sufficiently small impact parameter to overcome the potential barrier and approach the singularity.

IV. REGULARIZED NAKED SINGULARITY

The investigation of photon trajectories in the vicinity of Born-Infeld singularities, as denoted by Eq. (22), reveals an intriguing observation—photons can reach the singularity within a finite coordinate time. This phenomenon prompts a thorough examination of the fate of photons at the singularities as perceived by distant observers. However, the presence of a singularity signifies a breakdown in general relativity and its predictive capabilities. It is widely believed that a quantum theory of gravity would supersede general relativity at sufficiently small length scales, resolving this singularity issue. However, the absence of a fully established quantum gravity framework necessitates alternative approaches. Over the years, researchers have explored various effective models to “regularize” singularities, leading to several intriguing proposals, such as semiclassical loop quantum black holes [124], renormalization group improved black holes [125,126], rotating regular black hole solutions [127–132] and the application of the Simpson and Visser method [133]. Furthermore, a significant study has proposed that singularities can be smoothed out by considering the complete α' corrections of string theory [134–136].

Effective models frequently introduce one or more additional parameters to regularize the central singularity, incorporating a nonsingular core. This allows for studying the behavior of geodesics (particle paths) near the singularity. Beyond the nonsingular core, the original singularity spacetime closely approximates the regularized singularity spacetime. Similarly, a tiny nonsingular core can be introduced to remedy the singularity in the Born-Infeld metric, establishing a connection between ingoing and outgoing branches of photon trajectories. The right panel of Fig. 2 shows the Penrose diagram of a regularized Born-Infeld naked singularity with such a core, illustrating its causal structure. The red line depicts a radial light ray originating at past null infinity and propagating to future null infinity. Thanks to the nonsingular core, the light ray can traverse the regularized center at $r = 0$. It’s noteworthy that radial light rays follow radial null geodesics of the background metric, given that their effective metric and the background metric are conformally related.

To simplify our analysis, we construct a regularized Born-Infeld naked singularity spacetime by matching the original metric with a regular core centered at $r = 0$. This involves introducing a thin shell with a small but non-zero radius ϵ. Within this thin shell, the metric adopts the following form:

$$ds_{\mathrm{in}}^2 = -f_{\mathrm{in}}(r)dt^2 + \frac{dr^2}{h_{\mathrm{in}}(r)} + R_{\mathrm{in}}(r)(d\theta^2 + \sin^2\theta d\varphi^2), \quad (25)$$

where the metric functions are expanded as

$$\begin{aligned} f_{\mathrm{in}}(r) &= f_0 + f_1 r + \mathcal{O}(r^2), \\ h_{\mathrm{in}}(r) &= h_0 + h_1 r + \mathcal{O}(r^2), \\ R_{\mathrm{in}}(r) &= r^2[R_0 + R_1 r + \mathcal{O}(r^2)]. \end{aligned} \quad (26)$$

To avoid a conical singularity at $r = 0$, we require $h_0^{-1} = R_0$.

Furthermore, we assume that the electric and magnetic charges within the thin shell are spherically symmetric and smoothly distributed. The associated field strength tensor takes the form,

$$F_{\mu\nu} = \partial_\mu A_\nu - \partial_\nu A_\mu + \epsilon^{\rho\sigma}{}_{\mu\nu}\partial_\rho C_\sigma, \quad (27)$$

where a new gauge field C_μ is introduced due to the magnetic distribution [137]. The electric and magnetic fields E and B are then related to the strength tensor as

$$E_i = F^{i0}, \qquad B_i = \epsilon^{i0\rho\sigma}F_{\rho\sigma}.$$

Given our assumptions of regularity and spherical symmetry, the electric and magnetic fields assume the form,

$$\begin{aligned} E_r(r) &= -A_t'(r) = E_1 r + E_2 r^2 + \mathcal{O}(r^3), \\ B_r(r) &= -C_t'(r) = B_1 r + B_2 r^2 + \mathcal{O}(r^3). \end{aligned} \tag{28}$$

Substituting Eqs. (25) and (28) into Eq. (11) yields the effective metric within the thin shell,

$$d\tilde{s}^2_{\rm in} = -\tilde{f}_{\rm in}(r)dt^2 + \frac{dr^2}{\tilde{h}_{\rm in}(r)} + \tilde{R}_{\rm in}(r)(d\theta^2 + \sin^2\theta d\varphi^2), \tag{29}$$

with metric functions given by

$$\begin{aligned} \tilde{f}_{\rm in}(r) &= f_0 + \frac{a(B_1^2 - 3E_1^2)f_0^2}{2h_0}r^2 + \mathcal{O}(r^3), \\ \tilde{h}_{\rm in}(r) &= h_0 + \frac{a(3E_1^2 - B_1^2)f_0}{2}r^2 + \mathcal{O}(r^3), \\ \tilde{R}_{\rm in}(r) &= r^2\left[h_0^{-1} + \frac{a(3B_1^2 - E_1^2)f_0}{2h_0^2}r^2 + \mathcal{O}(r^3)\right]. \end{aligned} \tag{30}$$

When a light ray transitions from the Born-Infeld spacetime into the regular core, the energy $E_{\rm in}$ and angular momentum $L_{\rm in}$ within the regular core can be expressed in relation to the energy E and angular momentum L in the Born-Infeld spacetime, as detailed in [138,139],

$$E_{\rm in} = \frac{\tilde{f}_{\rm in}(\epsilon)}{f(\epsilon)}\sqrt{\frac{f_{\rm BI}(\epsilon)}{f_{\rm in}(\epsilon)}}E, \quad L_{\rm in} = \frac{\tilde{R}_{\rm in}(\epsilon)}{R(\epsilon)}\sqrt{\frac{\epsilon^2}{R_{\rm in}(\epsilon)}}L. \tag{31}$$

Given the spherical symmetry, we can confine the light ray to the equatorial plane, assuming its entry and exit from the thin shell occur at at $\varphi = \varphi_1$ and φ_2, respectively. Beyond the thin shell in the Born-Infeld spacetime, the trajectory of the light ray is governed by Eq. (24). This trajectory encompasses both ingoing and outgoing branches, with the former concluding at $\varphi = \varphi_1$ and the latter commencing from $\varphi = \varphi_2$ on the thin shell. The deflection angle $\Delta\varphi = \varphi_2 - \varphi_1$ that arises from the influence of the regular core is determined by the integral,

$$\Delta\varphi = 2\int_{r_0}^{\epsilon} \frac{\sqrt{\tilde{f}_{\rm in}(r)/\tilde{h}_{\rm in}(r)}}{\tilde{R}_{\rm in}(r)\sqrt{b_{\rm in}^{-2} - \tilde{f}_{\rm in}(r)/\tilde{R}_{\rm in}(r)}}dr, \tag{32}$$

where $r_0 = \sqrt{f_0 h_0}b_{\rm in}$ represents the turning point, and $b_{\rm in} = L_{\rm in}/E_{\rm in} \sim \epsilon^{7/2}$. As the shell radius ϵ approaches zero, the deflection angle asymptotically approaches π,

$$\Delta\varphi \to 2\ \arccos\left(\frac{\sqrt{k}b}{a(P^2+Q^2)}\epsilon^{5/2}\right) \to \pi, \tag{33}$$

where $k = \frac{\Gamma^2(1/4)[a(P^2+Q^2)]^{3/4}}{3a\sqrt{\pi}} - 2M$. This indicates that the entry and exit points on the thin shell become antipodally opposite. Moreover, for infinitesimally small cores, the ray's trajectory within the thin shell can be neglected. Consequently, the light ray can be well approximated by combining the ingoing and outgoing branches in the Born-Infeld metric outside the thin shell. These branches intersect the thin shell at precisely two antipodal points, establishing a simple relation for any light ray,

$$\theta \to \pi - \theta, \qquad \varphi \to \varphi + \pi. \tag{34}$$

In summary, the condition (34), along with the conservation of E, L_z and L, determine the corresponding outgoing branch for any given ingoing branch.

V. RELATIVISTIC IMAGES

In this section, we explore the phenomenon of gravitational lensing caused by Born-Infeld naked singularities in the context of the strong deflection limit. Our analysis starts with determining the deflection angle, which allows us to derive the angular positions of relativistic images. We employ an idealized thin lens model that assumes a high degree of alignment among the source, lens and observer. The lens equation, as presented in [21], is expressed as

$$\beta = \vartheta - \frac{D_{LS}}{D_{OS}}\Delta\alpha, \tag{35}$$

where β represents the angular separation between the source and the lens, ϑ denotes the angular separation between the lens and the image, and $\Delta\alpha$ represents the offset of the deflection angle after accounting for all the windings experienced by the photon. Here, the distances D_{OL}, D_{LS} and D_{OS} correspond to the observer-lens, lens-source and observer-source distances, respectively.

For the sake of simplicity, we confine our analysis to the equatorial plane, taking advantage of the spherical symmetry. In the idealized model, the deflection angle $\alpha(b)$ is described by the following expression from [21],

$$\alpha(b) = I(b) - \pi, \tag{36}$$

where $I(b)$ represents the change in φ, and b denotes the impact parameter related to ϑ through the equation $b = D_{OL}\vartheta$. When a photon approaches a turning point at $r = r_0$ and then gets deflected towards a distant observer, the integral $I(b)$ is given by

$$I(b) = 2\int_{r_0}^{\infty} \frac{1}{\sqrt{h(r)R(r)[R(r)/(b^2 f(r)) - 1]}}dr. \tag{37}$$

Alternatively, if the photon passes through the singularity at $r=0$, the azimuthal angle φ increases by π, resulting in the expression,

$$I(b)=2\int_0^{\infty}\frac{1}{\sqrt{h(r)R(r)[R(r)/(b^2f(r))-1]}}dr+\pi. \tag{38}$$

In the strong deflection limit, the integral $I(b)$ diverges as the impact parameter b approaches the critical value b_c, which represents the impact parameter for photon trajectories on the photon sphere at $r=r_c$. By expanding $I(b)$ around $b=b_c$ (or, equivalently $r_0=r_c$), we can obtain $\alpha(b)$ in the strong deflection limit.

A. Single photon sphere

We first study strong gravitational lensing in a Born-Infeld naked singularity with a single photon sphere. When the impact parameter of photons approaches the critical value, whether from below or above, they undergo significant deflections. It is important to highlight that photons can traverse the naked singularity if their impact parameter is smaller than b_c. Moreover, photons can orbit the photon sphere in either a clockwise or counterclockwise direction. Consequently, a distant source yields four relativistic images of nth-order, where n is a specified value.

Photons with $b>b_c$ reach a turning point r_0, located just outside the photon sphere r_c, as depicted by the red lines in Fig. 3. In such cases, the deflection angle in the regime of strong lensing is described by the equation [140,141]

$$\alpha(b)=-\bar{a}\ln(b/b_c-1)+\bar{b}+\mathcal{O}((b/b_c-1)\ln(b/b_c-1)), \tag{39}$$

where

$$\bar{a}=\sqrt{\frac{2f(r_c)}{h(r_c)[R''(r_c)f(r_c)-R(r_c)f''(r_c)]}},$$
$$\bar{b}=\bar{a}\ln\left[r_c^2\left(\frac{R''(r_c)}{R(r_c)}-\frac{f''(r_c)}{f(r_c)}\right)\right]+I_R(r_c)-\pi. \tag{40}$$

Here, the term $I_R(r_c)$ represents a regular integral that can be computed numerically. In the idealized lens model, the angular position of the image is related to the impact parameter by $b=D_{OL}\vartheta$. By utilizing the deflection angle formula (39) in conjunction with the lens equation (35), one can solve for the angular position $\vartheta^{>}_{\pm n}$ for nth-order relativistic images produced by photons orbiting the photon sphere n times. It is noteworthy that $-$ and $+$ in the subscript of $\vartheta^{>}_{\pm n}$ signify counterclockwise and clockwise orbits,

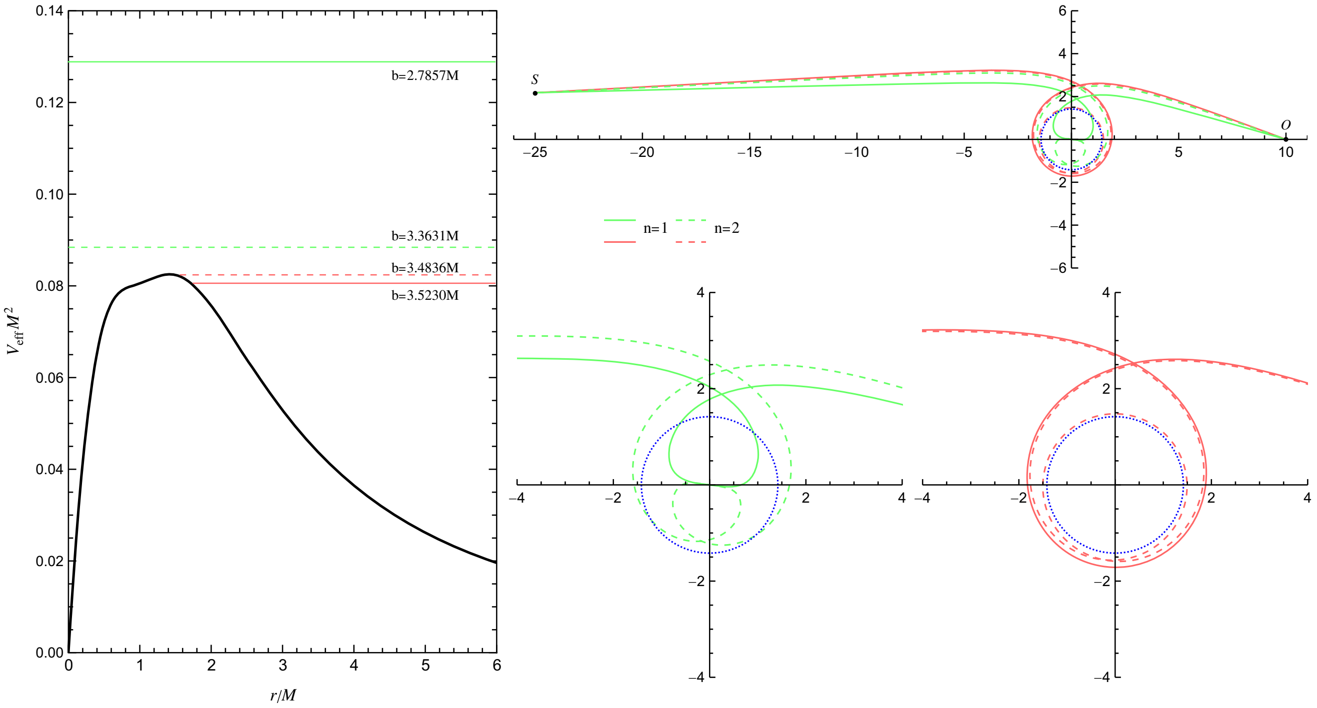

FIG. 3. Left: The effective potential of a Born-Infeld naked singularity with $\sqrt{P^2+Q^2}/M=1.2$ and $a/M^2=2$. It exhibits a single peak corresponding to a photon sphere at $r_c=1.4179M$ with the critical impact parameter $b_c=3.4811M$. The horizontal lines denote b^{-2} of light rays in the right panel. Right: Light rays connecting the source S with the observer O. The red and green lines represent light rays with $b>b_c$ and $b<b_c$, respectively. The light rays with $b<b_c$ pass through the singularity and generate relativistic images inside the critical curve in the image plane. The blue dashed lines depict the photon sphere, while the solid and dashed lines illustrate light rays orbiting once and twice around the photon sphere, respectively.

respectively, while the superscript > indicates photons with $b > b_c$. Specifically, the angular position $\vartheta^{>}_{\pm n}$ is given by [140]

$$\vartheta^{>}_{\pm n} = \vartheta^{>0}_{\pm n} + \frac{b_c e_n D_{OS}}{\bar{a} D_{LS} D_{OL}} (\beta - \vartheta^{>0}_{\pm n}), \tag{41}$$

where $e_n = e^{\frac{\bar{b}-2\pi n}{\bar{a}}}$, and $\vartheta^{>0}_{\pm n}$, satisfying $\alpha(\vartheta^{>0}_{\pm n}) = \pm 2n\pi$, is given by

$$\vartheta^{>0}_{n} = -\vartheta^{>0}_{-n} = \frac{b_c}{D_{OL}} (1 + e_n). \tag{42}$$

When $b < b_c$, photons emitted from the source can pass through the singularity, resulting in the generation of relativistic images within the critical curve, as depicted by the green lines in Fig. 3. To facilitate the derivation of the integral (38), we introduce a variable z defined as

$$z = 1 - \frac{2r_c}{r + r_c}. \tag{43}$$

The integral $I(b)$ can then be expressed as

$$I(b) = \int_{-1}^{1} A(z) D(z, b) dz, \tag{44}$$

where

$$\begin{aligned} A(z) &= \frac{4r_c}{(1-z)^2 R(r)} \sqrt{\frac{R(r_c) f(r)}{h(r)}}, \\ D(z, b) &= \frac{1}{\sqrt{R(r_c)/b^2 - f(r) R(r_c)/R(r)}}. \end{aligned} \tag{45}$$

Note that $A(z)$ is a regular function of z, whereas $D(z, b)$ diverges at $z = 0$ as $b \to b_c$. Hence, we decompose the integral $I(b)$ into a divergent part $I_D(b)$ and a regular part $I_R(b)$, as follows:

$$\begin{aligned} I_D(b) &= \int_{-1}^{1} A(0) D_0(z, b) dz, \\ I_R(b) &= \int_{-1}^{1} \left[A(z) D(z, b) - A(0) D_0(z, b_c) \right] dz. \end{aligned} \tag{46}$$

Here, we employ a Taylor expansion within the square root in $D(z, b)$ to obtain

$$D_0(z, b_c) = \frac{1}{\sqrt{\gamma + \eta z^2}}, \tag{47}$$

where γ and η are the expansion coefficients. Consequently, the divergent part $I_D(b)$ is given by

$$I_D(b) = \frac{A(0)}{\sqrt{\eta}} \ln \left[\frac{\eta + \sqrt{\eta(\gamma + \eta)}}{-\eta + \sqrt{\eta(\gamma + \eta)}} \right]. \tag{48}$$

Since the coefficient γ approaches zero as $b \to b_c$, the deflection angle in the strong limit is obtained by expanding $I_D(b)$ around $b = b_c$,

$$\alpha(b) = -\bar{a} \ln(b_c^2/b^2 - 1) + \bar{b} + \mathcal{O}((b_c/b - 1) \ln(b_c/b - 1)), \tag{49}$$

where

$$\begin{aligned} \bar{a} &= 2\sqrt{\frac{2f(r_c)}{h(r_c)[R''(r_c) f(r_c) - R(r_c) f''(r_c)]}}, \\ \bar{b} &= \bar{a} \ln \left[8r_c^2 \left(\frac{R''(r_c)}{R(r_c)} - \frac{f''(r_c)}{f(r_c)} \right) \right] + I_R(b_c). \end{aligned} \tag{50}$$

Similarly, the angular position of nth-order relativistic images is given by

$$\vartheta^{<}_{\pm n} = \vartheta^{<0}_{\pm n} - \frac{b_c e_n D_{OS}}{2\bar{a} D_{LS} D_{OL}} \frac{(\beta - \vartheta^{<0}_{\pm n})}{(1 + e_n)^{3/2}}, \tag{51}$$

where the angles $\vartheta^{<0}_{n}$ and $\vartheta^{<0}_{-n}$ are defined as

TABLE I. The angular separation $\Delta\vartheta^{\gtrless}_{\pm n} = \vartheta^{\gtrless}_{\pm n} - \vartheta^{0}_{\pm\infty}$ between nth-order relativistic images and the relativistic image formed at the photon sphere in Born-Infeld naked singularities with a single photon sphere. The parameters $\sqrt{P^2 + Q^2}/M = 1.2$ and $a/M^2 = 0.2$, 1.5 and 2 are considered. The values $M = 4.31 \times 10^6 M_\odot$, $D_{OL} = D_{LS} = 7.86$ kpc and $\beta = 2°$ are used. The superscripts > and < represent images produced by light rays with $b > b_c$ and $b < b_c$, respectively. The subscripts $+n$ and $-n$ indicate images produced by light rays orbiting around the photon sphere in the clockwise and counterclockwise direction, respectively. All angles are expressed in units of microarcseconds.

a/M^2	0.2	1.5	2
$\vartheta_{\pm\infty}$	± 4.1781	± 15.8189	± 18.9161
$\Delta\vartheta^{>}_{1}$	1.0663×10^{-24}	1.1386	0.2334
$\Delta\vartheta^{>}_{2}$	2.1968×10^{-47}	3.4876×10^{-7}	1.0560×10^{-2}
$\Delta\vartheta^{>}_{3}$	4.5259×10^{-70}	1.0682×10^{-13}	4.7773×10^{-4}
$\Delta\vartheta^{<}_{1}$	-3.0217×10^{-7}	-9.4142	-2.9161
$\Delta\vartheta^{<}_{2}$	-1.3715×10^{-18}	-2.2188×10^{-2}	-0.7526
$\Delta\vartheta^{<}_{3}$	-6.2252×10^{-30}	-1.2305×10^{-5}	-0.1679
$\Delta\vartheta^{>}_{-1}$	-2.8311×10^{-25}	-0.8133	-0.2179
$\Delta\vartheta^{>}_{-2}$	-5.8325×10^{-48}	-2.4912×10^{-7}	-9.8579×10^{-3}
$\Delta\vartheta^{>}_{-3}$	-1.2016×10^{-70}	-7.6304×10^{-14}	-4.4596×10^{-4}
$\Delta\vartheta^{<}_{-1}$	1.6624×10^{-7}	8.9587	2.8385
$\Delta\vartheta^{<}_{-2}$	7.5453×10^{-19}	1.8780×10^{-2}	0.7286
$\Delta\vartheta^{<}_{-3}$	3.4248×10^{-30}	1.0412×10^{-5}	0.1623

$$\vartheta_n^{<0} = -\vartheta_{-n}^{<0} = \frac{b_c}{D_{OL}}\frac{1}{\sqrt{1+e_n}}. \tag{52}$$

To obtain numerical estimations of $\vartheta_{\pm n}^{\gtrless}$ in an astrophysical setting, we consider a Born-Infeld naked singularity with parameters corresponding to the supermassive black hole Sgr A* located at the center of our Galaxy. Specifically, we assume a mass of $M = 4.31 \times 10^6 M_\odot$ and a lens-source distance of $D_{OL} = 7.86$ kpc. Additionally, a source is positioned at $D_{LS} = 7.86$ kpc with an angular separation of $\beta = 2°$. For Born-Infeld naked singularities with $\sqrt{P^2+Q^2}/M = 1.2$ and various values of a/M^2, Table I presents $\Delta\vartheta_{\pm n}^{\gtrless} \equiv \vartheta_{\pm n}^{\gtrless} - \vartheta_{\pm\infty}$, where $\vartheta_{\pm\infty} = \lim_{n\to\infty}\vartheta_{\pm n}^{\gtrless 0} = \pm b_c/D_{OL}$ is the angular position of the relativistic image formed at the photon sphere. Note that the corresponding effective potentials of the singularities are displayed in Figs. 1 and 3. The results demonstrate that as the nonlinear parameter a increases, the potential peak becomes less pronounced, leading to larger values of $\Delta\vartheta_{\pm n}^{\gtrless}$. This, in turn, facilitates the resolution of higher-order relativistic images. Moreover, the relativistic images with $b < b_c$ are more widely separated compared to those with $b > b_c$ due to the significant bending of light rays upon entering or exiting the photon sphere. Considering a resolution of 0.01 microarcseconds, which is capable of resolving the first-order relativistic image in a Schwarzschild black hole [95,140,142], it is observed that relativistic images associated with the singularity having $a/M^2 = 0.2$ are too closely spaced to be resolved. However, all $n = 1$ relativistic images of the singularity with $a/M^2 = 1.5$, as well as $n \leq 3$ images of the singularity with $a/M^2 = 2$, can be distinguished.

B. Double photon spheres

In the presence of a Born-Infeld naked singularity with a double-peak effective potential, two photon spheres are observed at distinct locations, namely, $r = r_{\text{in}}$ and $r = r_{\text{out}}$, with $r_{\text{in}} < r_{\text{out}}$. The critical impact parameters b_{in} and b_{out} represent the impact parameter of light rays on the inner and outer, respectively. If the height of the inner potential peak is lower than that of the outer peak, the inner photon sphere remains invisible to a distant observer, resulting in gravitational lensing similar to the single-peak scenario. However, when the height of the inner peak surpasses that of the outer peak, a distant source can generate a total of eight nth-order relativistic images due to strong gravitational lensing near the inner and outer photon spheres. The light rays responsible for these relativistic images are categorized based on their impact parameter b,

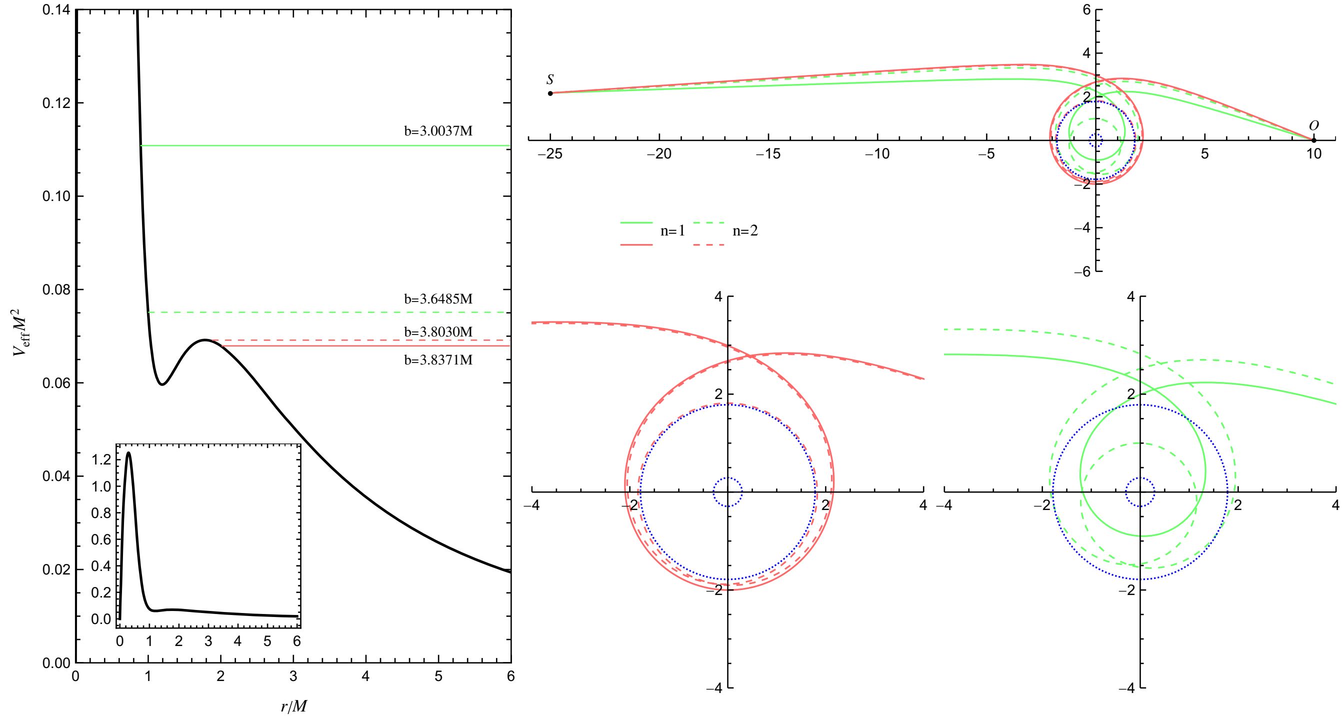

FIG. 4. Left: The effective potential of a Born-Infeld naked singularity with $\sqrt{P^2+Q^2}/M = 1.2$ and $a/M^2 = 0.2$. Notably, it displays two peaks corresponding to the inner photon sphere at $r_{\text{in}} = 0.2919M$ and the outer one at $r_{\text{out}} = 1.7833M$. The horizontal lines denote b^{-2} of light rays in the right panel, which undergo significant lensing effects near the outer photon sphere with the impact parameter $b_{\text{out}} = 3.8021M$. Right: Light rays are depicted by red and green lines, indicating those with $b > b_{\text{out}}$ and $b < b_{\text{out}}$, respectively. The blue dashed lines represent the photon spheres, while the solid and dashed lines demonstrate light rays orbiting once and twice around the outer photon sphere, respectively.

(i) For $b < b_{\text{in}}$, depicted by the green lines in Fig. 3, where the potential peak is treated as the inner one. The light rays emitted from the source pass through the singularity and produce two relativistic images at $\vartheta = \vartheta_{\pm n}^{\text{in}<}$, with the minus $(-)$ and plus $(+)$ signs representing the counterclockwise and clockwise directions, respectively.

(ii) For $b > b_{\text{in}}$, illustrated by the red lines in Fig. 3. The light rays reach a turning point r_0 just outside the inner photon sphere before escaping towards the observer, generating two relativistic images at $\vartheta = \vartheta_{\pm n}^{\text{in}>}$.

(iii) For $b < b_{\text{out}}$, shown by the green lines in Fig. 4. The light rays are reflected at $r = r_0$ by the potential barrier between the two photon spheres, producing two relativistic images at $\vartheta = \vartheta_{\pm n}^{\text{out}<}$.

(iv) For $b > b_{\text{out}}$, demonstrated by the red lines in Fig. 4. The light rays reach a turning point r_0 slightly outside the outer photon sphere, resulting in two relativistic images at $\vartheta = \vartheta_{\pm n}^{\text{out}>}$.

Note that the angular position of the images, $\vartheta_{\pm n}^{\text{out}>,\text{in}>}$ and $\vartheta_{\pm n}^{\text{in}<}$, can be computed using Eqs. (41) and (51), respectively. Moreover, the deflection angle of light rays with $b < b_{\text{out}}$ has been previously shown to be [95]

$$\alpha(b) = -\bar{a}\log\left(b_{\text{out}}^2/b^2 - 1\right) + \bar{b} + \mathcal{O}((b_{\text{out}}/b - 1)\ln(b_{\text{out}}/b - 1)), \tag{53}$$

where

$$\bar{a} = 2\sqrt{\frac{2f(r_m)}{h(r_{\text{out}})[R''(r_m)f(r_m) - R(r_m)f''(r_m)]}},$$
$$\bar{b} = \bar{a}\log\left[r_m^2\left(\frac{r_m}{r_{\text{out}}} - 1\right)\left(\frac{R''(r_m)}{R(r_m)} - \frac{f''(r_m)}{f(r_m)}\right)\right] + I_R(r_{\text{out}}) - \pi. \tag{54}$$

Here, r_m is the critical turning point when b is very close to b_{out}. Since the divergent parts of the deflection angles (49) and (53) share the same form, one can utilize Eq. (51) to calculate $\vartheta_{\pm n}^{\text{out}<}$ with the values of $\bar{a}$ and $\bar{b}$ from Eq. (54).

TABLE II. Angular separation of relativistic images near the inner and outer critical curves in Born-Infeld naked singularities with double photon spheres. The parameters M, D_{OL}, D_{LS}, β and $\sqrt{P^2 + Q^2}/M$ are chosen to be consistent with those presented in Table I. *Left*: The angular separation $\Delta\vartheta_{\pm n}^{\text{in}\gtrless} = \vartheta_{\pm n}^{\text{in}\gtrless} - \vartheta_{\pm\infty}^{\text{in}}$ between nth-order relativistic images near the inner critical curve and the relativistic image formed at the inner photon sphere. *Right*: The angular separation $\Delta\vartheta_{\pm n}^{\text{out}\gtrless} = \vartheta_{\pm n}^{\text{out}\gtrless} - \vartheta_{\pm\infty}^{\text{out}}$ between nth-order relativistic images near the outer critical curve and the relativistic image formed at the outer photon sphere.

a/M^2	0.2	1
$\vartheta_{\pm\infty}^{\text{in}}$	± 4.8562	± 17.6478
$\Delta\vartheta_{1}^{\text{in}>}$	1.0197×10^{-25}	81.9543
$\Delta\vartheta_{2}^{\text{in}>}$	1.4343×10^{-51}	1.2180×10^{-20}
$\Delta\vartheta_{3}^{\text{in}>}$	2.0176×10^{-77}	1.8100×10^{-42}
$\Delta\vartheta_{1}^{\text{in}<}$	-6.1033×10^{-7}	-17.6186
$\Delta\vartheta_{2}^{\text{in}<}$	-7.2387×10^{-20}	-3.7064×10^{-5}
$\Delta\vartheta_{3}^{\text{in}<}$	-8.5853×10^{-33}	-4.5184×10^{-16}
$\Delta\vartheta_{-1}^{\text{in}>}$	-2.0781×10^{-26}	-23.2197
$\Delta\vartheta_{-2}^{\text{in}>}$	-2.9232×10^{-52}	-3.4508×10^{-21}
$\Delta\vartheta_{-3}^{\text{in}>}$	-4.1120×10^{-78}	-5.1283×10^{-43}
$\Delta\vartheta_{-1}^{\text{in}<}$	3.0698×10^{-7}	17.6091
$\Delta\vartheta_{-2}^{\text{in}<}$	3.6408×10^{-20}	2.0884×10^{-5}
$\Delta\vartheta_{-3}^{\text{in}<}$	4.3181×10^{-33}	2.5459×10^{-16}

a/M^2	0.2	1	1.5
$\vartheta_{\pm\infty}^{\text{out}}$	± 20.6602	± 21.4264	± 21.7967
$\Delta\vartheta_{1}^{\text{out}>}$	0.2415	0.1491	0.1198
$\Delta\vartheta_{2}^{\text{out}>}$	6.5113×10^{-3}	1.6409×10^{-3}	9.6643×10^{-4}
$\Delta\vartheta_{3}^{\text{out}>}$	1.7553×10^{-4}	1.8056×10^{-5}	7.7952×10^{-6}
$\Delta\vartheta_{1}^{\text{out}<}$	-4.6237	-4.6184	-7.5266
$\Delta\vartheta_{2}^{\text{out}<}$	-1.0356	-0.6696	-1.1980
$\Delta\vartheta_{3}^{\text{out}<}$	-0.1813	-7.3293×10^{-2}	-0.1162
$\Delta\vartheta_{-1}^{\text{out}>}$	-0.2229	-0.1349	-0.1076
$\Delta\vartheta_{-2}^{\text{out}>}$	-6.0086×10^{-3}	-1.4843×10^{-3}	-8.6817×10^{-4}
$\Delta\vartheta_{-3}^{\text{out}>}$	-1.6198×10^{-4}	-1.6333×10^{-5}	-7.0027×10^{-6}
$\Delta\vartheta_{-1}^{\text{out}<}$	4.4968	4.4581	7.3092
$\Delta\vartheta_{-2}^{\text{out}<}$	0.9977	0.6383	1.1403
$\Delta\vartheta_{-3}^{\text{out}<}$	0.1743	6.9728×10^{-2}	0.1102

Similarly, in the aforementioned astrophysical scenario of Born-Infeld naked singularities with a single photon sphere, the angular positions of the relativistic images can be estimated numerically. Specifically, we present the values of $\Delta\vartheta_{\pm n}^{\text{in}\gtrless} \equiv \vartheta_{\pm n}^{\text{in}\gtrless} - \vartheta_{\pm\infty}^{\text{in}}$ and $\Delta\vartheta_{\pm n}^{\text{out}\gtrless} \equiv \vartheta_{\pm n}^{\text{out}\gtrless} - \vartheta_{\pm\infty}^{\text{out}}$ for $a/M^2 = 0.2$, 1 and 1.5 in Table II. Here, $\vartheta_{\pm\infty}^{\text{in}}$ and $\vartheta_{\pm\infty}^{\text{out}}$ are the angular positions of the relativistic images formed at the inner and outer photon spheres, respectively. We also assume a resolution of 0.01 microarcseconds, which enables the resolution of the first-order image in a Schwarzschild black hole. For a singularity with $a/M^2 = 0.2$, the inner potential peak is significantly sharper and higher than the outer peak. Consequently, the relativistic images at $\vartheta = \vartheta_{\pm n}^{\text{in}\gtrless}$ are closely situated near the inner critical curve at $\vartheta = \vartheta_{\pm\infty}^{\text{in}}$, making them indistinguishable on the image plane. However, the images near the outer critical curve at $\vartheta = \vartheta_{\pm\infty}^{\text{out}}$ are well-separated from the outer critical curve, allowing for the distinction of the first-order images with $b > b_{\text{out}}$ and the first three orders ($n \leq 3$) images with $b < b_{\text{out}}$. When $a/M^2 = 1$, the inner potential peak becomes flatter, resulting in greater separation among the images near the inner critical curve. It should be emphasized that, due to the inner potential peak not being significantly higher than the outer peak, the formulas for $\vartheta_{\pm n}^{\mathrm{in}>}$ and $\vartheta_{\pm n}^{\mathrm{out}<}$ in the strong deflection limit may exhibit substantial errors. For the singularity with $a/M^2 = 1.5$, the inner peak is lower than the outer peak, leading to the existence of relativistic images solely near the outer critical curve.

VI. CELESTIAL SPHERE IMAGES

In this section, we investigate gravitational lensing by a Born-Infeld naked singularity through the image of a luminous celestial sphere centered at the singularity and surrounding the observers. To obtain the image of the celestial sphere, we use the numerical backward ray-tracing method to calculate light rays from the observer to the celestial sphere. Light rays can be described either by numerically integrating Eq. (18) or eight first-order differential equations

$$\frac{dx^\mu}{d\lambda} = p^\mu,$$
$$\frac{dp^\mu}{d\lambda} = -\tilde{\Gamma}^\mu_{\rho\sigma} p^\rho p^\sigma, \tag{55}$$

where λ represents the affine parameter, and $\tilde{\Gamma}^\mu_{\rho\sigma}$ are the Christoffel symbols compatible with the effective metric. Numerically solving Eq. (55) for light rays enables us to avoid the need to account for turning points during the integration, resulting in improved numerical accuracy. Thus, we use Eq. (55) to calculate the light rays connecting the observer with the celestial sphere.

For a static observer located at $(t_o, r_o, \theta_o, \varphi_o)$, we introduce a tetrad basis

$$e_{(t)} = \frac{\partial_t}{\sqrt{-g_{tt}(r_o,\theta_o)}}, \quad e_{(r)} = \frac{\partial_r}{\sqrt{g_{rr}(r_o,\theta_o)}},$$
$$e_{(\theta)} = \frac{\partial_\theta}{\sqrt{g_{\theta\theta}(r_o,\theta_o)}}, \quad e_{(\varphi)} = \frac{\partial_\varphi}{\sqrt{g_{\varphi\varphi}(r_o,\theta_o)}}, \tag{56}$$

which span the tangent bundle at the observer. To obtain initial conditions for Eq. (55), a photon captured by the observer is considered, whose local 4-momentum $(p^{(t)}, p^{(r)}, p^{(\theta)}, p^{(\varphi)})$ in the tetrad basis is related to the 4-momentum $p_o^\mu = dx^\mu/d\lambda|_{(t_o,r_o,\theta_o,\varphi_o)}$ as

$$p^{(t)} = \sqrt{f_{\mathrm{BI}}(r_o)}\, p_o^t, \qquad p^{(r)} = p_o^r / \sqrt{f_{\mathrm{BI}}(r_o)},$$
$$p^{(\theta)} = r_o p_o^\theta, \qquad p^{(\varphi)} = r_o |\sin\theta_o| p_o^\varphi. \tag{57}$$

The observation angles Θ and Φ, as defined in [143], are given by

$$\sin\Theta = \frac{p^{(\theta)}}{p}, \qquad \tan\Phi = \frac{p^{(\varphi)}}{p^{(r)}}, \tag{58}$$

which $p = \sqrt{p^{(r)2} + p^{(\theta)2} + p^{(\varphi)2}}$. We express $p^{(r)}$, $p^{(\theta)}$ and $p^{(\varphi)}$ in terms of p, Θ and Φ as

$$p^{(r)} = p\cos\Theta\cos\Phi, \quad p^{(\theta)} = p\sin\Theta, \quad p^{(\phi)} = p\cos\Theta\sin\Phi. \tag{59}$$

Moreover, the condition $\tilde{g}_{\mu\nu} p_o^\mu p_o^\nu = 0$ and Eq. (57) give

$$p^{(t)} = p\sqrt{\frac{f_{\mathrm{BI}}(r_o)}{f(r_o)}}\sqrt{\frac{f_{\mathrm{BI}}(r_o)}{h(r_o)}\cos^2\Theta\cos^2\Phi + \frac{R(r_o)}{r_o^2}(\sin^2\Theta + \sin^2\Phi\cos^2\Theta)}. \tag{60}$$

Using Eq. (57), we can rewrite p_o^μ in terms of p, Θ and Φ, which, together with the coordinates of the observer, provide initial conditions for Eq. (55). Without loss of generality, we set $p = 1$ in what follows. The Cartesian coordinates (x, y) of the image plane of the observer is defined by

$$x \equiv -r_o\Phi, \qquad y \equiv r_o\Theta, \tag{61}$$

where the sign convention for Φ leads to the minus sign in the x definition. Note that the direction pointing to the singularity corresponds to the zero observation angles (0, 0).

As discussed previously, when a light ray travels through the singularity, its affine parameter λ becomes divergent at $r = 0$, posing a challenge for our numerical implementation. To circumvent this issue, we introduce a small sphere of radius $M\epsilon$ to enclose the singularity. Outside the sphere, we can solve Eq. (55) numerically, ensuring the accuracy and stability of the light ray calculation. Within the sphere, we can use the expansions in Eq. (23) to describe the light ray and provide a connection formula for its entry and exit points from the sphere. Specifically, we consider the light ray entering and leaving the sphere at $(t_{\mathrm{in}}, r_{\mathrm{in}}, \theta_{\mathrm{in}}, \varphi_{\mathrm{in}})$ and $(t_{\mathrm{out}}, r_{\mathrm{out}}, \theta_{\mathrm{out}}, \varphi_{\mathrm{out}})$, respectively. With Eqs. (24) and (34), one has

$$t_{\mathrm{out}} = t_{\mathrm{in}} + \mathcal{O}(\epsilon^2), \qquad r_{\mathrm{out}} = r_{\mathrm{in}} = M\epsilon, \qquad \theta_{\mathrm{out}} = \pi - \theta_{\mathrm{in}} + \mathcal{O}(\epsilon^3), \qquad \varphi_{\mathrm{out}} = \pi + \varphi_{\mathrm{in}} + \mathcal{O}(\epsilon^3),$$
$$p^t_{\mathrm{out}} = p^t_{\mathrm{in}}, \qquad p^r_{\mathrm{out}} = -p^r_{\mathrm{in}}, \qquad p^\theta_{\mathrm{out}} = -p^\theta_{\mathrm{in}} + \mathcal{O}(\epsilon^5 \log\epsilon), \qquad p^\varphi_{\mathrm{out}} = p^\varphi_{\mathrm{in}} + \mathcal{O}(\epsilon^5 \log\epsilon). \tag{62}$$

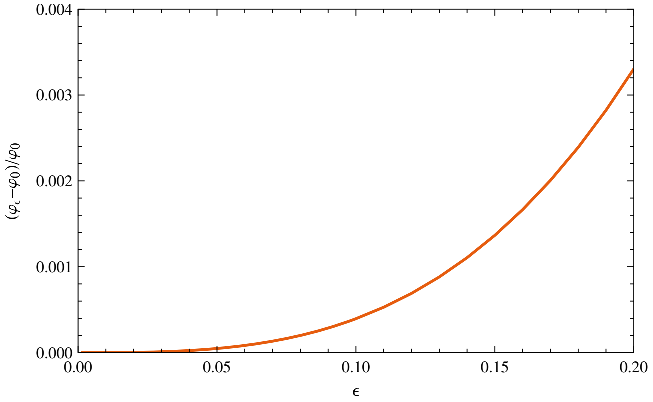

FIG. 5. The relative error $(\varphi_\epsilon - \varphi_0)/\varphi_0$ as a function of ϵ for a light ray emitted from $(r_e, \varphi_e) = (25M, \varphi_\epsilon)$ and arriving at $(r_o, \varphi_o) = (10M, \pi)$ with $(\Theta, \Phi) = (0, 3/20)$ on the equatorial plane. The light ray passes through the singularity, and the ingoing and outgoing branches are joined at $r = M\epsilon$ during numerical calculations. Here, $\varphi_0 = \varphi_{\epsilon=10^{-3}}$, $a/M^2 = 1$ and $\sqrt{Q^2 + P^2}/M = 1.05$.

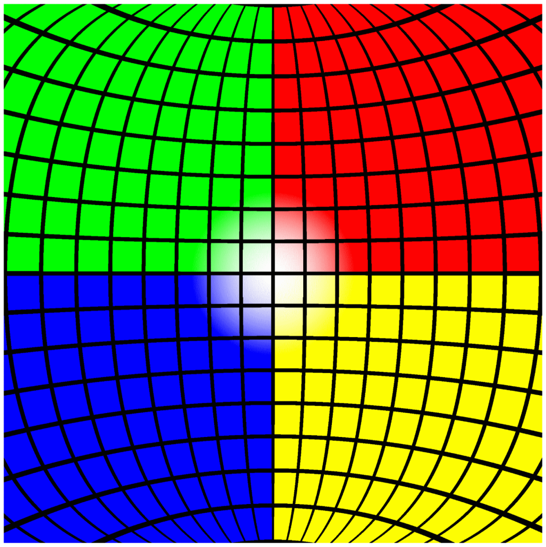

FIG. 6. Observational image of the celestial sphere in the Minkowski spacetime. The observer is positioned at $x_o^\mu = (0, 10M, \pi/2, \pi)$ with a field of view of $2\pi/3$.

In this section, we employ the leading terms of Eq. (62) to connect the ingoing and outgoing branches. To explore the numerical error caused by the finite size of ϵ, we investigate a light ray on the equatorial plane of a Born-Infeld naked singularity with $a/M^2 = 1$ and $\sqrt{Q^2 + P^2}/M = 1.05$. The light ray originates from $(r_e, \varphi_e) = (25M, \varphi_\epsilon)$, and an observer located at $(r_o, \varphi_o) = (10M, \pi)$ captures it with observation angles $(\Theta, \Phi) = (0, 3/20)$. To obtain the coordinate φ_ϵ, we trace the light ray backward from the observer to $r_e = 25M$ while connecting the ingoing branch with the outgoing one at $r = M\epsilon$. We present the relative error $(\varphi_\epsilon - \varphi_0)/\varphi_0$ as a function of ϵ in Fig. 5, where $\varphi_0 \equiv \varphi_{\epsilon=10^{-3}}$. To maintain numerical precision and efficiency, we set $\epsilon = 10^{-1}$ in the following numerical simulations, for which the relative error is well below 10^{-3}.

To illustrate gravitational lensing by Born-Infeld naked singularities, we position a luminous celestial sphere at $r_{\mathrm{CS}} = 25M$, while an observer is situated at $x_o^\mu = (0, 10M, \pi/2, \pi)$. The celestial sphere is divided into four quadrants, each distinguished by a different color, and a white dot is placed in front of the observer. Additionally, we overlay a grid of black lines representing constant longitude and latitude, where adjacent lines are separated by $\pi/18$. To generate an observational image, we vary the observer's viewing angle and numerically integrate 2000×2000 photon trajectories until they intersect with the celestial sphere.

Figure 7 displays images of the celestial sphere in both RN and Born-Infeld naked singularities, both of which possess a single photon sphere. The dashed circular lines in the images correspond to the critical curve formed by light rays originating from the photon sphere. Beyond this critical curve, the images of the celestial sphere in naked singularities bear resemblance to those observed in black hole spacetime. Notably, unlike shadows observed in black hole images, the celestial sphere images persist within the critical curve due to the absence of an event horizon. Additionally, higher-order images of the celestial sphere can be observed both inside and outside this critical curve.

The left panel of Fig. 7 illustrates the image of the celestial sphere in a RN naked singularity characterized by $\sqrt{Q^2 + P^2}/M = 1.05$. Inside the critical curve, three distinct white rings can be observed. These rings correspond to the Einstein ring generated by the white dot positioned on the celestial sphere. Specifically, the innermost white ring originates from light rays emitted by the white dot, undergoes reflection at the potential barrier, and eventually reaches the observer after experiencing an angular coordinate change of $\Delta\varphi = \pi$. Within this innermost white ring, the reflections from the infinitely high potential barrier at the singularity produce a mirror image of the celestial sphere. Moreover, the middle and outermost white rings arise from light rays with angular coordinate changes of $\Delta\varphi = 3\pi$ and 5π, respectively. In the right panel of Fig. 7, the image captured in a Born-Infeld naked singularity with $\sqrt{Q^2 + P^2}/M = 1.2$ and $a/M^2 = 2$ is displayed. As expected, light rays passing through the singularity and undergoing an angular coordinate change of $\Delta\varphi = \pi$ result in a white dot positioned at the center of the image. Additionally, two white rings emerge within the critical curve, representing photons that traverse the singularity with angular coordinate changes of $\Delta\varphi = 3\pi$ and 5π, respectively.

Figure 8 showcases images of the celestial sphere in Born-Infeld naked singularities featuring two photon

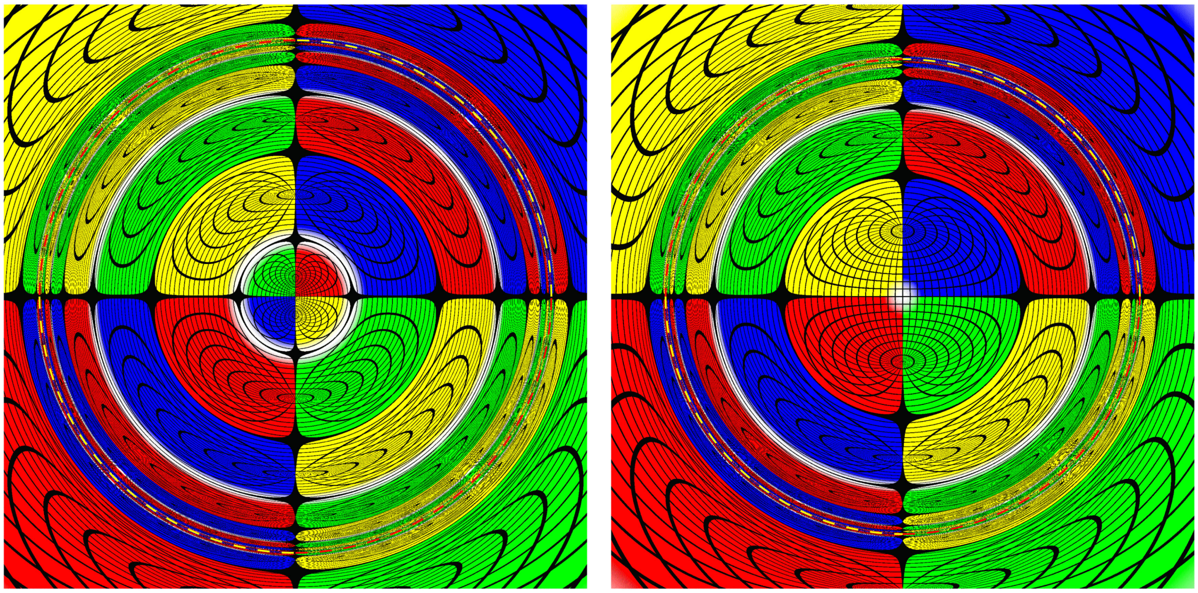

FIG. 7. Images of the celestial sphere in naked singularities featuring a single photon sphere. The observer is situated at $x_o^\mu = (0, 10M, \pi/2, \pi)$ with a field of view of $\pi/4$. The dashed lines depict the critical curve formed by photons escaping from the photon sphere. Left: The RN naked singularity with $\sqrt{Q^2 + P^2}/M = 1.05$. The image within the critical curve is generated by light rays that rebound off the infinitely high potential barrier at the singularity. Three white rings, representing the Einstein ring of the white dot on the celestial sphere, can be observed within the critical curve. Right: The Born-Infeld naked singularity with $\sqrt{Q^2 + P^2}/M = 1.2$ and $a/M^2 = 2$. The image within the critical curve is formed by light rays passing through the singularity. A central white dot is visible, surrounded by two white rings.

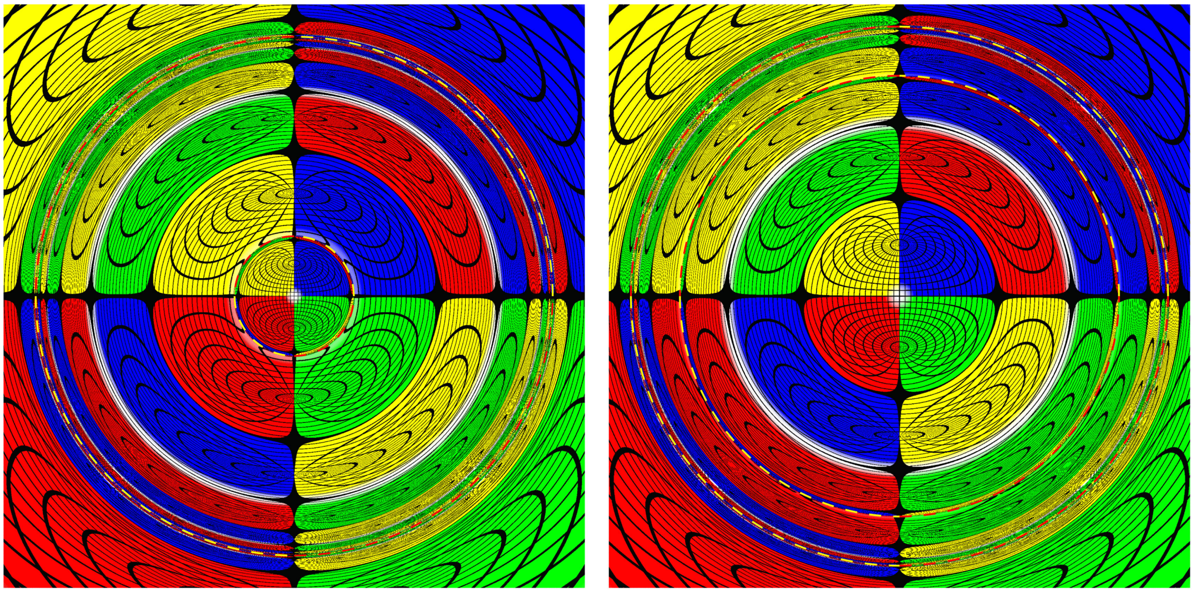

FIG. 8. Images of the celestial sphere in Born-Infeld naked singularities with $\sqrt{Q^2 + P^2}/M = 1.05$ for $a/M^2 = 0.2$ (left) and $a/M^2 = 1$ (right), featuring both inner and outer photon spheres. The observer is located at $x_o^\mu = (0, 10M, \pi/2, \pi)$ with a field of view of $\pi/4$, and the corresponding inner and outer critical curves are represented by dashed lines. The image within the inner critical curve is formed by light rays traversing the singularity, while the image between the inner and outer critical curves is a result of light rays reflecting off the potential barrier situated between the inner and outer potential peaks.

spheres. The inner and outer photon spheres give rise to corresponding inner and outer critical curves, as indicated by the dashed lines in the images. Higher-order celestial sphere images are observed on both sides of these critical curves. Similarly to the case of a single photon sphere, a central white spot appears in the images due to the transparency of the Born-Infeld naked singularity. In the left panel, characterized by $\sqrt{Q^2+P^2}/M = 1.05$ and $a/M^2 = 0.2$, two white rings can be observed positioned between the inner and outer critical curves. These rings originate from photons that are reflected by the potential barrier located between the inner and outer potential peaks with $\Delta\varphi = 3\pi$ and 5π. In the right panel, with $\sqrt{Q^2+P^2}/M = 1.05$ and $a/M^2 = 1.5$, a white ring emerges between the two critical curves. This ring arises from photons that undergo reflection at the potential barrier with an angular coordinate change of $\Delta\varphi = 5\pi$. Additionally, a white ring is observed inside the inner critical curve, which occurs due to photons passing through the singularity and experiencing an angular coordinate change of $\Delta\varphi = 3\pi$.

This analysis assumes an observer-lens distance D_{OL} of $10M$, significantly smaller than the actual distances from Earth to Sgr A* ($3.80 \times 10^{10}M$) and M87* ($5.39 \times 10^{10}M$). Consequently, Figs. (6–8) display much larger fields of view compared to what Earth-based observers would capture. To estimate the field of view for Earth-based observations, we can leverage the Cartesian image plane coordinates (x, y) defined in Eq. (61). These coordinates, exhibiting minimal dependence on D_{OL}, provide a robust measure of the observed region. Figure 6 portrays the image of the celestial sphere in Minkowski spacetime with a field of view of $2\pi/3$, corresponding to a Cartesian coordinate range of $20\pi M/3$. For Earth-based observers, this translates to roughly 113.68 microarcseconds for Sgr A* and 80.21 microarcseconds for M87*. Similarly, Figs. 7 and 8 depict a field of view of $\pi/4$ (Cartesian coordinate range: $5\pi M/2$), resulting in approximately 42.63 microarcseconds for Sgr A* and 30.07 microarcseconds for M87* for Earth-based observations.

The current EHT possesses an angular resolution of approximately 25 microarcseconds, hindering the ability to discern features within the celestial sphere images presented here. However, the next-generation EHT holds the promise of a substantial enhancement in angular resolution, expected to improve by up to 50% to approximately 15 microarcseconds [144,145]. This advancement has the potential to discern finer features in these images. Additionally, space-based Very Long Baseline Interferometry endeavors to achieve even higher angular resolution, aiming for 1 microarcsecond as outlined in [146,147]. This considerable enhancement will facilitate the resolution of additional details in these images.

VII. CONCLUSIONS

This paper investigated the phenomenon of gravitational lensing by Born-Infeld naked singularities, which are solutions of a $(3+1)$-dimensional gravity model coupled to a Born-Infeld electromagnetic field. Owing to the nonlinearity inherent in Born-Infeld electrodynamics, photons follow null geodesics of an effective metric, deviating from the background metric.Photons entering photon spheres from distant sources were remarkably observed to reach the singularity within a finite coordinate time. Under the assumption of a regular core resolving the singularity, these photons can traverse the regularized singularity, resulting in the formation of new images within critical curves. Additionally, we demonstrated that Born-Infeld naked singularities can exhibit the presence of two photon spheres with distinct sizes within specific parameter ranges. The existence of these double photon spheres, combined with the transparency of naked singularities, significantly impacts the gravitational lensing of light sources, leading to various effects such as the emergence of new relativistic images. Consequently, these findings provide a potent tool for detecting and studying Born-Infeld naked singularities through their distinctive gravitational lensing signatures.

Naked singularities with double photon spheres have been infrequently reported; however, it has been discovered that asymptotically flat black holes can possess two photon spheres outside the event horizon [114,117,148]. A recent investigation focused on studying the relativistic images produced by pointlike light sources and luminous celestial spheres in the presence of black holes with either a single or double photon spheres [118]. The key findings regarding strong gravitational lensing by black holes and naked singularities can be summarized as follows:

(i) Black holes with a single photon sphere: In the celestial sphere image, a shadow is observed enclosed by the critical curve, which originates from light rays escaping the photon sphere. For a pointlike source, two *n*th-order relativistic images are present just outside the critical curve, corresponding to clockwise and counterclockwise winding around the black hole.

(ii) Black holes with double photon spheres: The celestial sphere image exhibits both inner and outer critical curves, formed by the inner and outer photon spheres, respectively. Within the image, there exists a shadow enclosed by the inner critical curve. Two *n*th-order relativistic images of a pointlike source appear just outside the outer critical curve, two images are found just inside the outer critical curve, and two additional images emerge just outside the inner critical curve.

(iii) Born-Infeld naked singularities with a single photon sphere: The celestial sphere image lacks a shadow, and the image within the critical curve is formed by light rays passing through the singularity. For a pointlike source, there are four nth-order relativistic images, specifically, two images situated just inside the critical curve and two images positioned just outside the critical curve.

(iv) Born-Infeld naked singularities with double photon spheres: The celestial sphere image does not exhibit a shadow, and the image within the inner critical curve is produced by light rays that traverse the singularity. For a pointlike source, there are eight nth-order relativistic images, two images on each side of the inner and outer critical curves.

Within the uncertainties of the EHT observations, the captured images are consistent with those expected from a Kerr black hole, displaying a central brightness depression. Conversely, our theoretical model allows for light rays to traverse regularized Born-Infeld naked singularities, potentially resulting in the absence of such a central brightness depression in the corresponding images. This discrepancy could serve as compelling evidence against modeling M87* or Sgr A* as Born-Infeld naked singularities. However, it should be noted that the current observations only weakly constrain the depth of the central brightness depression. For instance, in the case of M87*, the center brightness is constrained to be no more than 10% of the average brightness in the surrounding ring [22]. This raises the question of whether this limited constraint still permits the possibility of regularized Born-Infeld naked singularities or could even be used to establish bounds on their parameters. To address this question definitively, numerical simulations of accretion disks around Born-Infeld naked singularities are required, followed by a comprehensive comparison with the EHT observations. We leave this important avenue of exploration for future research.

Although current observational facilities lack the capability to distinguish higher-order relativistic images within the Born-Infeld naked singularity spacetime, the next-generation Very Long Baseline Interferometry has emerged as a promising tool for this purpose [149–151]. Furthermore, it has been demonstrated that relativistic images located inside the critical curves are more readily detectable compared to those outside the critical curves. Hence, it would be highly intriguing if our analysis could be extended to encompass more astrophysically realistic models, such as the rotating Born-Infeld naked singularity solution and the imaging of accretion disks.

Finally, the particular regularization method in this paper enables us to observe images both within and outside the critical cure. However, it is noteworthy that the method used to regularize the singularity is not unique. Thus the optical appearances of distant sources depend on a specific regularization method. For instance, the singularity can also be regularized by a wormhole throat instead of a regular core [133], photons reaching the throat will traverse to another universe. Therefore, the resulting observational appearances of distant sources are dependent on the observer's position, whether it is in the same universe as the source. If the source and the observer reside in different universes, only images situated within the critical curve are able to be observed. Such observational phenomena distinct from those associated with black holes and worth further research in the future.

ACKNOWLEDGMENTS

We are grateful to Qingyu Gan and Xin Jiang for useful discussions and valuable comments. This work is supported in part by NSFC (Grants No. 12105191, No. 12275183, No. 12275184 and No. 11875196). Houwen Wu is supported by the International Visiting Program for Excellent Young Scholars of Sichuan University.

---

[1] F. W. Dyson, A. S. Eddington, and C. Davidson, A determination of the deflection of light by the sun's gravitational field, from observations made at the total eclipse of May 29, 1919, Phil. Trans. R. Soc. A **220**, 291 (1920).

[2] Albert Einstein, Lens-like action of a star by the deviation of light in the gravitational field, Science **84**, 506 (1936).

[3] A. S. Eddington, *Space, Time and Gravitation. An Outline of the General Relativity Theory* (Cambridge University Press, 1987).

[4] Yannick Mellier, Probing the universe with weak lensing, Annu. Rev. Astron. Astrophys. **37**, 127 (1999).

[5] Matthias Bartelmann and Peter Schneider, Weak gravitational lensing, Phys. Rep. **340**, 291 (2001).

[6] Catherine Heymans *et al.*, CFHTLenS tomographic weak lensing cosmological parameter constraints: Mitigating the impact of intrinsic galaxy alignments, Mon. Not. R. Astron. Soc. **432**, 2433 (2013).

[7] Nick Kaiser and Gordon Squires, Mapping the dark matter with weak gravitational lensing, Astrophys. J. **404**, 441 (1993).

[8] Douglas Clowe, Marusa Bradac, Anthony H. Gonzalez, Maxim Markevitch, Scott W. Randall, Christine Jones, and Dennis Zaritsky, A direct empirical proof of the existence of dark matter, Astrophys. J. Lett. **648**, L109 (2006).

[9] Farruh Atamurotov, Ahmadjon Abdujabbarov, and Wen-Biao Han, Effect of plasma on gravitational lensing by a

Schwarzschild black hole immersed in perfect fluid dark matter, Phys. Rev. D **104**, 084015 (2021).

[10] Marek Biesiada, Strong lensing systems as a probe of dark energy in the universe, Phys. Rev. D **73**, 023006 (2006).

[11] Shuo Cao, Marek Biesiada, Rapha Gavazzi, Aleksandra Piórkowska, and Zong-Hong Zhu, Cosmology with strong-lensing systems, Astrophys. J. **806**, 185 (2015).

[12] T. M. C. Abbott *et al.*, Dark Energy Survey Year 1 results: Cosmological constraints from cluster abundances and weak lensing, Phys. Rev. D **102**, 023509 (2020).

[13] T. M. C. Abbott *et al.*, Dark Energy Survey Year 3 results: Cosmological constraints from galaxy clustering and weak lensing, Phys. Rev. D **105**, 023520 (2022).

[14] Xiaohui Fan *et al.*, The discovery of a luminous $z = 5.80$ quasar from the Sloan Digital Sky Survey, Astron. J. **120**, 1167 (2000).

[15] Chien Y. Peng, Chris D. Impey, Hans-Walter Rix, Christopher S. Kochanek, Charles R. Keeton, Emilio E. Falco, Joseph Lehar, and Brian A. McLeod, Probing the coevolution of supermassive black holes and galaxies using gravitationally lensed quasar hosts, Astrophys. J. **649**, 616 (2006).

[16] Masamune Oguri and Philip J. Marshall, Gravitationally lensed quasars and supernovae in future wide-field optical imaging surveys, Mon. Not. R. Astron. Soc. **405**, 2579 (2010).

[17] Minghao Yue, Xiaohui Fan, Jinyi Yang, and Feige Wang, Revisiting the lensed fraction of high-redshift quasars, Astrophys. J. **925**, 169 (2022).

[18] Uros Seljak and Christopher M. Hirata, Gravitational lensing as a contaminant of the gravity wave signal in CMB, Phys. Rev. D **69**, 043005 (2004).

[19] Jose M. Diego, Tom Broadhurst, and George Smoot, Evidence for lensing of gravitational waves from LIGO-Virgo data, Phys. Rev. D **104**, 103529 (2021).

[20] Andreas Finke, Stefano Foffa, Francesco Iacovelli, Michele Maggiore, and Michele Mancarella, Probing modified gravitational wave propagation with strongly lensed coalescing binaries, Phys. Rev. D **104**, 084057 (2021).

[21] K. S. Virbhadra and George F. R. Ellis, Schwarzschild black hole lensing, Phys. Rev. D **62**, 084003 (2000).

[22] Kazunori Akiyama *et al.*, First M87 Event Horizon Telescope results. I. The shadow of the supermassive black hole, Astrophys. J. Lett. **875**, L1 (2019).

[23] Kazunori Akiyama *et al.*, First M87 Event Horizon Telescope results. II. Array and instrumentation, Astrophys. J. Lett. **875**, L2 (2019).

[24] Kazunori Akiyama *et al.*, First M87 Event Horizon Telescope results. III. Data processing and calibration, Astrophys. J. Lett. **875**, L3 (2019).

[25] Kazunori Akiyama *et al.*, First M87 Event Horizon Telescope results. IV. Imaging the central supermassive black hole, Astrophys. J. Lett. **875**, L4 (2019).

[26] Kazunori Akiyama *et al.*, First M87 Event Horizon Telescope results. V. Physical origin of the asymmetric ring, Astrophys. J. Lett. **875**, L5 (2019).

[27] Kazunori Akiyama *et al.*, First M87 Event Horizon Telescope results. VI. The shadow and mass of the central black hole, Astrophys. J. Lett. **875**, L6 (2019).

[28] Kazunori Akiyama *et al.*, First M87 Event Horizon Telescope results. VII. Polarization of the ring, Astrophys. J. Lett. **910**, L12 (2021).

[29] Kazunori Akiyama *et al.*, First M87 Event Horizon Telescope results. VIII. Magnetic field structure near the Event Horizon, Astrophys. J. Lett. **910**, L13 (2021).

[30] Kazunori Akiyama *et al.*, First Sagittarius A* Event Horizon Telescope results. I. The shadow of the supermassive black hole in the center of the milky way, Astrophys. J. Lett. **930**, L12 (2022).

[31] Kazunori Akiyama *et al.*, First Sagittarius A* Event Horizon Telescope results. II. EHT and multiwavelength observations, data processing, and calibration, Astrophys. J. Lett. **930**, L13 (2022).

[32] Kazunori Akiyama *et al.*, First Sagittarius A* Event Horizon Telescope results. III. Imaging of the galactic center supermassive black hole, Astrophys. J. Lett. **930**, L14 (2022).

[33] Kazunori Akiyama *et al.*, First Sagittarius A* Event Horizon Telescope results. IV. Variability, morphology, and black hole mass, Astrophys. J. Lett. **930**, L15 (2022).

[34] Kazunori Akiyama *et al.*, First Sagittarius A* Event Horizon Telescope results. V. Testing astrophysical models of the galactic center black hole, Astrophys. J. Lett. **930**, L16 (2022).

[35] Kazunori Akiyama *et al.*, First Sagittarius A* Event Horizon Telescope results. VI. Testing the black hole metric, Astrophys. J. Lett. **930**, L17 (2022).

[36] Heino Falcke, Fulvio Melia, and Eric Agol, Viewing the shadow of the black hole at the galactic center, Astrophys. J. Lett. **528**, L13 (2000).

[37] Clarissa-Marie Claudel, K. S. Virbhadra, and G. F. R. Ellis, The geometry of photon surfaces, J. Math. Phys. (N.Y.) **42**, 818 (2001).

[38] Ernesto F. Eiroa, Gustavo E. Romero, and Diego F. Torres, Reissner-Nordstrom black hole lensing, Phys. Rev. D **66**, 024010 (2002).

[39] K. S. Virbhadra, Relativistic images of Schwarzschild black hole lensing, Phys. Rev. D **79**, 083004 (2009).

[40] Akifumi Yumoto, Daisuke Nitta, Takeshi Chiba, and Naoshi Sugiyama, Shadows of multi-black holes: Analytic exploration, Phys. Rev. D **86**, 103001 (2012).

[41] Shao-Wen Wei and Yu-Xiao Liu, Observing the shadow of Einstein-Maxwell-Dilaton-Axion black hole, J. Cosmol. Astropart. Phys. 11 (2013) 063.

[42] Alexander F. Zakharov, Constraints on a charge in the Reissner-Nordström metric for the black hole at the Galactic Center, Phys. Rev. D **90**, 062007 (2014).

[43] Farruh Atamurotov, Sushant G. Ghosh, and Bobomurat Ahmedov, Horizon structure of rotating Einstein–Born–Infeld black holes and shadow, Eur. Phys. J. C **76**, 273 (2016).

[44] Sara Dastan, Reza Saffari, and Saheb Soroushfar, Shadow of a Kerr-Sen dilaton-axion black hole, arXiv:1610.09477.

[45] Pedro V. P. Cunha, Carlos A. R. Herdeiro, Burkhard Kleihaus, Jutta Kunz, and Eugen Radu, Shadows of Einstein–dilaton–Gauss–Bonnet black holes, Phys. Lett. B **768**, 373 (2017).

[46] Mingzhi Wang, Songbai Chen, and Jiliang Jing, Shadow casted by a Konoplya-Zhidenko rotating non-Kerr black hole, J. Cosmol. Astropart. Phys. 10 (2017) 051.

[47] Muhammed Amir, Balendra Pratap Singh, and Sushant G. Ghosh, Shadows of rotating five-dimensional charged EMCS black holes, Eur. Phys. J. C **78**, 399 (2018).

[48] Ali Övgün, İzzet Sakallı, and Joel Saavedra, Shadow cast and deflection angle of Kerr-Newman-Kasuya spacetime, J. Cosmol. Astropart. Phys. 10 (2018) 041.

[49] Volker Perlick, Oleg Yu. Tsupko, and Gennady S. Bisnovatyi-Kogan, Black hole shadow in an expanding universe with a cosmological constant, Phys. Rev. D **97**, 104062 (2018).

[50] Tao Zhu, Qiang Wu, Mubasher Jamil, and Kimet Jusufi, Shadows and deflection angle of charged and slowly rotating black holes in Einstein-Æther theory, Phys. Rev. D **100**, 044055 (2019).

[51] Cosimo Bambi, Katherine Freese, Sunny Vagnozzi, and Luca Visinelli, Testing the rotational nature of the supermassive object M87* from the circularity and size of its first image, Phys. Rev. D **100**, 044057 (2019).

[52] Akash K. Mishra, Sumanta Chakraborty, and Sudipta Sarkar, Understanding photon sphere and black hole shadow in dynamically evolving spacetimes, Phys. Rev. D **99**, 104080 (2019).

[53] Sunny Vagnozzi and Luca Visinelli, Hunting for extra dimensions in the shadow of M87*, Phys. Rev. D **100**, 024020 (2019).

[54] Rahul Kumar, Sushant G. Ghosh, and Anzhong Wang, Shadow cast and deflection of light by charged rotating regular black holes, Phys. Rev. D **100**, 124024 (2019).

[55] Liang Ma and H. Lu, Bounds on photon spheres and shadows of charged black holes in Einstein-Gauss-Bonnet-Maxwell gravity, Phys. Lett. B **807**, 135535 (2020).

[56] Alireza Allahyari, Mohsen Khodadi, Sunny Vagnozzi, and David F. Mota, Magnetically charged black holes from non-linear electrodynamics and the Event Horizon Telescope, J. Cosmol. Astropart. Phys. 02 (2020) 003.

[57] Xiao-Xiong Zeng, Hai-Qing Zhang, and Hongbao Zhang, Shadows and photon spheres with spherical accretions in the four-dimensional Gauss–Bonnet black hole, Eur. Phys. J. C **80**, 872 (2020).

[58] Xiao-Xiong Zeng and Hai-Qing Zhang, Influence of quintessence dark energy on the shadow of black hole, Eur. Phys. J. C **80**, 1058 (2020).

[59] Rittick Roy and Sayan Chakrabarti, Study on black hole shadows in asymptotically de Sitter spacetimes, Phys. Rev. D **102**, 024059 (2020).

[60] Peng-Cheng Li, Minyong Guo, and Bin Chen, Shadow of a spinning black hole in an expanding universe, Phys. Rev. D **101**, 084041 (2020).

[61] Rahul Kumar, Sushant G. Ghosh, and Anzhong Wang, Gravitational deflection of light and shadow cast by rotating Kalb-Ramond black holes, Phys. Rev. D **101**, 104001 (2020).

[62] Sunny Vagnozzi, Cosimo Bambi, and Luca Visinelli, Concerns regarding the use of black hole shadows as standard rulers, Classical Quantum Gravity **37**, 087001 (2020).

[63] Mohsen Khodadi, Alireza Allahyari, Sunny Vagnozzi, and David F. Mota, Black holes with scalar hair in light of the Event Horizon Telescope, J. Cosmol. Astropart. Phys. 09 (2020) 026.

[64] Abhishek Chowdhuri and Arpan Bhattacharyya, Shadow analysis for rotating black holes in the presence of plasma for an expanding universe, Phys. Rev. D **104**, 064039 (2021).

[65] K. Saurabh and Kimet Jusufi, Imprints of dark matter on black hole shadows using spherical accretions, Eur. Phys. J. C **81**, 490 (2021).

[66] Ming Zhang and Jie Jiang, Shadows of accelerating black holes, Phys. Rev. D **103**, 025005 (2021).

[67] Subhodeep Sarkar, Shailesh Kumar, and Srijit Bhattacharjee, Can we detect a supertranslated black hole?, Phys. Rev. D **105**, 084001 (2022).

[68] Merce Guerrero, Gonzalo J. Olmo, Diego Rubiera-Garcia, and Diego Gómez Sáez-Chillón, Light ring images of double photon spheres in black hole and wormhole spacetimes, Phys. Rev. D **105**, 084057 (2022).

[69] K. S. Virbhadra, Distortions of images of Schwarzschild lensing, Phys. Rev. D **106**, 064038 (2022).

[70] Sunny Vagnozzi *et al.*, Horizon-scale tests of gravity theories and fundamental physics from the Event Horizon Telescope image of Sagittarius A^*, Classical Quantum Gravity **40**, 165007 (2023).

[71] Abhishek Chowdhuri, Saptaswa Ghosh, and Arpan Bhattacharyya, A review on analytical studies in gravitational lensing, Front. Phys. **11**, 1113909 (2023).

[72] Fabian Schmidt, Weak lensing probes of modified gravity, Phys. Rev. D **78**, 043002 (2008).

[73] Jacek Guzik, Bhuvnesh Jain, and Masahiro Takada, Tests of gravity from imaging and spectroscopic surveys, Phys. Rev. D **81**, 023503 (2010).

[74] Kai Liao, Zhengxiang Li, Shuo Cao, Marek Biesiada, Xiaogang Zheng, and Zong-Hong Zhu, The distance duality relation from strong gravitational lensing, Astrophys. J. **822**, 74 (2016).

[75] Prieslei Goulart, Phantom wormholes in Einstein–Maxwell-dilaton theory, Classical Quantum Gravity **35**, 025012 (2018).

[76] J. R. Nascimento, A. Yu. Petrov, P. J. Porfirio, and A. R. Soares, Gravitational lensing in black-bounce spacetimes, Phys. Rev. D **102**, 044021 (2020).

[77] Xin Qin, Songbai Chen, and Jiliang Jing, Image of a regular phantom compact object and its luminosity under spherical accretions, Classical Quantum Gravity **38**, 115008 (2021).

[78] Shafqat Ul Islam, Jitendra Kumar, and Sushant G. Ghosh, Strong gravitational lensing by rotating Simpson-Visser black holes, J. Cosmol. Astropart. Phys. 10 (2021) 013.

[79] Naoki Tsukamoto, Gravitational lensing by two photon spheres in a black-bounce spacetime in strong deflection limits, Phys. Rev. D **104**, 064022 (2021).

[80] Haroldo C. D. Lima Junior, Jian-Zhi Yang, Luís C. B. Crispino, Pedro V. P. Cunha, and Carlos A. R. Herdeiro, Einstein-Maxwell-dilaton neutral black holes in strong magnetic fields: Topological charge, shadows, and lensing, Phys. Rev. D **105**, 064070 (2022).

[81] Gonzalo J. Olmo, Diego Rubiera-Garcia, and Diego Sáez-Chillón Gómez, New light rings from multiple critical curves as observational signatures of black hole mimickers, Phys. Lett. B **829**, 137045 (2022).

[82] Saptaswa Ghosh and Arpan Bhattacharyya, Analytical study of gravitational lensing in Kerr-Newman black-bounce spacetime, J. Cosmol. Astropart. Phys. 11 (2022) 006.

[83] Stuart L. Shapiro and Saul A. Teukolsky, Formation of naked singularities: The violation of cosmic censorship, Phys. Rev. Lett. **66**, 994 (1991).

[84] P. S. Joshi and I. H. Dwivedi, Naked singularities in spherically symmetric inhomogeneous Tolman-Bondi dust cloud collapse, Phys. Rev. D **47**, 5357 (1993).

[85] Tomohiro Harada, Hideo Iguchi, and Ken-ichi Nakao, Naked singularity formation in the collapse of a spherical cloud of counter rotating particles, Phys. Rev. D **58**, 041502 (1998).

[86] Pankaj S. Joshi, Naresh Dadhich, and Roy Maartens, Why do naked singularities form in gravitational collapse?, Phys. Rev. D **65**, 101501 (2002).

[87] Rituparno Goswami and Pankaj S. Joshi, Spherical gravitational collapse in N-dimensions, Phys. Rev. D **76**, 084026 (2007).

[88] Narayan Banerjee and Soumya Chakrabarti, Self-similar scalar field collapse, Phys. Rev. D **95**, 024015 (2017).

[89] Kaushik Bhattacharya, Dipanjan Dey, Arindam Mazumdar, and Tapobrata Sarkar, New class of naked singularities and their observational signatures, Phys. Rev. D **101**, 043005 (2020).

[90] K. S. Virbhadra and G. F. R. Ellis, Gravitational lensing by naked singularities, Phys. Rev. D **65**, 103004 (2002).

[91] K. S. Virbhadra and C. R. Keeton, Time delay and magnification centroid due to gravitational lensing by black holes and naked singularities, Phys. Rev. D **77**, 124014 (2008).

[92] Galin N. Gyulchev and Stoytcho S. Yazadjiev, Gravitational lensing by rotating naked singularities, Phys. Rev. D **78**, 083004 (2008).

[93] Satyabrata Sahu, Mandar Patil, D. Narasimha, and Pankaj S. Joshi, Can strong gravitational lensing distinguish naked singularities from black holes?, Phys. Rev. D **86**, 063010 (2012).

[94] Pritam Banerjee, Suvankar Paul, and Tapobrata Sarkar, On strong gravitational lensing in rotating galactic spacetimes, arXiv:1804.07030.

[95] Rajibul Shaikh, Pritam Banerjee, Suvankar Paul, and Tapobrata Sarkar, Analytical approach to strong gravitational lensing from ultracompact objects, Phys. Rev. D **99**, 104040 (2019).

[96] Suvankar Paul, Strong gravitational lensing by a strongly naked null singularity, Phys. Rev. D **102**, 064045 (2020).

[97] Naoki Tsukamoto, Gravitational lensing by a photon sphere in a Reissner-Nordström naked singularity spacetime in strong deflection limits, Phys. Rev. D **104**, 124016 (2021).

[98] M. Born and L. Infeld, Foundations of the new field theory, Proc. R. Soc. A **144**, 425 (1934).

[99] Tanay Kr. Dey, Born-Infeld black holes in the presence of a cosmological constant, Phys. Lett. B **595**, 484 (2004).

[100] Rong-Gen Cai, Da-Wei Pang, and Anzhong Wang, Born-Infeld black holes in (A)dS spaces, Phys. Rev. D **70**, 124034 (2004).

[101] Sharmanthie Fernando and Don Krug, Charged black hole solutions in Einstein-Born-Infeld gravity with a cosmological constant, Gen. Relativ. Gravit. **35**, 129 (2003).

[102] Rabin Banerjee, Sumit Ghosh, and Dibakar Roychowdhury, New type of phase transition in Reissner Nordström–AdS black hole and its thermodynamic geometry, Phys. Lett. B **696**, 156 (2011).

[103] De-Cheng Zou, Shao-Jun Zhang, and Bin Wang, Critical behavior of Born-Infeld AdS black holes in the extended phase space thermodynamics, Phys. Rev. D **89**, 044002 (2014).

[104] Seyed Hossein Hendi, Behzad Eslam Panah, and Shahram Panahiyan, Einstein-Born-Infeld-massive gravity: AdS-black hole solutions and their thermodynamical properties, J. High Energy Phys. 11 (2015) 157.

[105] Xiao-Xiong Zeng, Xian-Ming Liu, and Li-Fang Li, Phase structure of the Born–Infeld–anti-de Sitter black holes probed by non-local observables, Eur. Phys. J. C **76**, 616 (2016).

[106] Shoulong Li, H. Lu, and Hao Wei, Dyonic (A)dS black holes in Einstein-Born-Infeld theory in diverse dimensions, J. High Energy Phys. 07 (2016) 004.

[107] Jun Tao, Peng Wang, and Haitang Yang, Testing holographic conjectures of complexity with Born–Infeld black holes, Eur. Phys. J. C **77**, 817 (2017).

[108] Amin Dehyadegari and Ahmad Sheykhi, Reentrant phase transition of Born-Infeld-AdS black holes, Phys. Rev. D **98**, 024011 (2018).

[109] Peng Wang, Houwen Wu, and Haitang Yang, Thermodynamics and phase transitions of nonlinear electrodynamics black holes in an extended phase space, J. Cosmol. Astropart. Phys. 04 (2019) 052.

[110] Qingyu Gan, Guangzhou Guo, Peng Wang, and Houwen Wu, Strong cosmic censorship for a scalar field in a Born-Infeld–de Sitter black hole, Phys. Rev. D **100**, 124009 (2019).

[111] Peng Wang, Houwen Wu, and Haitang Yang, Thermodynamics and phase transition of a nonlinear electrodynamics black hole in a cavity, J. High Energy Phys. 07 (2019) 002.

[112] Kangkai Liang, Peng Wang, Houwen Wu, and Mingtao Yang, Phase structures and transitions of Born–Infeld black holes in a grand canonical ensemble, Eur. Phys. J. C **80**, 187 (2020).

[113] Peng Wang, Houwen Wu, and Haitang Yang, Scalarized Einstein-Born-Infeld black holes, Phys. Rev. D **103**, 104012 (2021).

[114] Guangzhou Guo, Yuhang Lu, Peng Wang, Houwen Wu, and Haitang Yang, Black holes with multiple photon spheres, Phys. Rev. D **107**, 124037 (2023).

[115] M. Novello, V. A. De Lorenci, J. M. Salim, and Renato Klippert, Geometrical aspects of light propagation in nonlinear electrodynamics, Phys. Rev. D **61**, 045001 (2000).

[116] Qingyu Gan, Peng Wang, Houwen Wu, and Haitang Yang, Photon ring and observational appearance of a hairy black hole, Phys. Rev. D **104**, 044049 (2021).

[117] Qingyu Gan, Peng Wang, Houwen Wu, and Haitang Yang, Photon spheres and spherical accretion image of a hairy black hole, Phys. Rev. D **104**, 024003 (2021).

[118] Guangzhou Guo, Xin Jiang, Peng Wang, and Houwen Wu, Gravitational lensing by black holes with multiple photon spheres, Phys. Rev. D **105**, 124064 (2022).

[119] Yiqian Chen, Guangzhou Guo, Peng Wang, Houwen Wu, and Haitang Yang, Appearance of an infalling star in black holes with multiple photon spheres, Sci. China Phys. Mech. Astron. **65**, 120412 (2022).

[120] Guangzhou Guo, Peng Wang, Houwen Wu, and Haitang Yang, Quasinormal modes of black holes with multiple photon spheres, J. High Energy Phys. 06 (2022) 060.

[121] Guangzhou Guo, Peng Wang, Houwen Wu, and Haitang Yang, Echoes from hairy black holes, J. High Energy Phys. 06 (2022) 073.

[122] Guangzhou Guo, Peng Wang, Houwen Wu, and Haitang Yang, Superradiance instabilities of charged black holes in Einstein-Maxwell-scalar theory, J. High Energy Phys. 07 (2023) 070.

[123] D. Pugliese, H. Quevedo, and R. Ruffini, Circular motion of neutral test particles in Reissner-Nordström spacetime, Phys. Rev. D **83**, 024021 (2011).

[124] Leonardo Modesto, Semiclassical loop quantum black hole, Int. J. Theor. Phys. **49**, 1649 (2010).

[125] Alfio Bonanno and Martin Reuter, Renormalization group improved black hole space-times, Phys. Rev. D **62**, 043008 (2000).

[126] Alessia Platania, Dynamical renormalization of black-hole spacetimes, Eur. Phys. J. C **79**, 470 (2019).

[127] Cosimo Bambi and Leonardo Modesto, Rotating regular black holes, Phys. Lett. B **721**, 329 (2013).

[128] Mustapha Azreg-Aïnou, Generating rotating regular black hole solutions without complexification, Phys. Rev. D **90**, 064041 (2014).

[129] Bobir Toshmatov, Bobomurat Ahmedov, Ahmadjon Abdujabbarov, and Zdenek Stuchlik, Rotating regular black hole solution, Phys. Rev. D **89**, 104017 (2014).

[130] Astrid Eichhorn and Aaron Held, Image features of spinning regular black holes based on a locality principle, Eur. Phys. J. C **81**, 933 (2021).

[131] Héloïse Delaporte, Astrid Eichhorn, and Aaron Held, Parameterizations of black-hole spacetimes beyond circularity, Classical Quantum Gravity **39**, 134002 (2022).

[132] Rajes Ghosh, Mostafizur Rahman, and Akash K. Mishra, Regularized stable Kerr black hole: Cosmic censorships, shadow and quasi-normal modes, Eur. Phys. J. C **83**, 91 (2023).

[133] Kunal Pal, Kuntal Pal, Pratim Roy, and Tapobrata Sarkar, Regularizing the JNW and JMN naked singularities, Eur. Phys. J. C **83**, 397 (2023).

[134] Peng Wang, Houwen Wu, Haitang Yang, and Shuxuan Ying, Non-singular string cosmology via α' corrections, J. High Energy Phys. 10 (2019) 263.

[135] Peng Wang, Houwen Wu, Haitang Yang, and Shuxuan Ying, Construct α' corrected or loop corrected solutions without curvature singularities, J. High Energy Phys. 01 (2020) 164.

[136] Shuxuan Ying, Resolving naked singularities in α'-corrected string theory, Eur. Phys. J. C **82**, 523 (2022).

[137] N. Cabibbo and E. Ferrari, Quantum electrodynamics with Dirac monopoles, Nuovo Cimento **23**, 1147 (1962).

[138] Xiaobao Wang, Peng-Cheng Li, Cheng-Yong Zhang, and Minyong Guo, Novel shadows from the asymmetric thin-shell wormhole, Phys. Lett. B **811**, 135930 (2020).

[139] Yiqian Chen, Peng Wang, Houwen Wu, and Haitang Yang, Observational appearance of a freely-falling star in an asymmetric thin-shell wormhole, Eur. Phys. J. C **83**, 361 (2023).

[140] V. Bozza, Gravitational lensing in the strong field limit, Phys. Rev. D **66**, 103001 (2002).

[141] Naoki Tsukamoto, Deflection angle in the strong deflection limit in a general asymptotically flat, static, spherically symmetric spacetime, Phys. Rev. D **95**, 064035 (2017).

[142] Shao-Wen Wei, Ke Yang, and Yu-Xiao Liu, Black hole solution and strong gravitational lensing in Eddington-inspired Born–Infeld gravity, Eur. Phys. J. C **75**, 253 (2015); **75**, 331(E) (2015).

[143] Pedro V. P. Cunha, Carlos A. R. Herdeiro, Eugen Radu, and Helgi F. Runarsson, Shadows of Kerr black holes with and without scalar hair, Int. J. Mod. Phys. D **25**, 1641021 (2016).

[144] Sheperd S. Doeleman *et al.*, Reference array and design consideration for the next-generation Event Horizon Telescope, Galaxies **11**, 107 (2023).

[145] Michael D. Johnson *et al.*, Key science goals for the next-generation Event Horizon Telescope, Galaxies **11**, 61 (2023).

[146] Leonid I. Gurvits *et al.*, THEZA: TeraHertz exploration and zooming-in for astrophysics: An ESA Voyage 2050 White Paper, Exp. Astron. **51**, 559 (2021).

[147] Leonid I. Gurvits *et al.*, The science case and challenges of space-borne sub-millimeter interferometry, Acta Astronaut. **196**, 314 (2022).

[148] Hai-Shan Liu, Zhan-Feng Mai, Yue-Zhou Li, and H. Lü, Quasi-topological electromagnetism: Dark energy, dyonic black holes, stable photon spheres and hidden electromagnetic duality, Sci. China Phys. Mech. Astron. **63**, 240411 (2020).

[149] Michael D. Johnson *et al.*, Universal interferometric signatures of a black hole's photon ring, Sci. Adv. **6**, eaaz1310 (2020).

[150] Elizabeth Himwich, Michael D. Johnson, Alexandru Lupsasca, and Andrew Strominger, Universal polarimetric signatures of the black hole photon ring, Phys. Rev. D **101**, 084020 (2020).

[151] Samuel E. Gralla, Alexandru Lupsasca, and Daniel P. Marrone, The shape of the black hole photon ring: A precise test of strong-field general relativity, Phys. Rev. D **102**, 124004 (2020).